

Crustal structure of the East-African Limpopo Margin, a strike-slip rifted corridor along the continental Mozambique Coastal Plain and North-Natal Valley

Mikael Evain¹, Philippe Schnürle¹, Angélique Leprêtre^{1,2}, Fanny Verrier¹, Louise Watremez³, Joseph Offei Thompson¹, Philippe de Clarens⁴, Daniel Aslanian¹, and Maryline Moulin¹

¹IFREMER, Geosciences Marines, REM/GM/LGS, Centre de Brest, 29280 Plouzané, France

²LGO, IUEM, Place Nicolas Copernic, 29280 Plouzané, France

³Univ. Lille, CNRS, Univ. Littoral Côte d'Opale, UMR 8187 – LOG – Laboratoire d'Océanologie et de Géosciences, F-59000 Lille, France

⁴TOTAL, R&D, avenue Larribau, 64000 Pau, France

Correspondence: Mikael Evain (mikael.evain@ifremer.fr)

Abstract.

Coincident wide-angle and multi-channel seismic data acquired within the scope of the PAMELA Moz3-5 project allow to reconsider the formation mechanism of East-African margins offshore southern Mozambique. This study most specifically focuses on the sedimentary and deep crustal architecture of the Limpopo margin (LM) that fringes the eastern edge of the Mozambique's Coastal Plain (MCP) and its offshore southern prolongation the North Natal Valley (NNV). It relies primarily on the MZ3 profile that runs obliquely from the northeastern NNV towards the Mozambique basin (MB) with additional inputs from a tectono-stratigraphy analysis of industrial onshore-offshore seismic lines and nearby or crossing velocity models from companion studies. Over its entire N-S extension the LM appears segmented in (1) a western domain that shows the progressive eastward crustal thinning and termination of the MCP/NNV continental crust and its overlying pre-Neocomien volcano-sedimentary basement; and (2) a central corridor of anomalous crust bounded to the east by the Mozambique fracture zone (MFZ) and the oceanic crust of the MB. A prominent basement high marks the boundary between these two domains. Its development was most probably controlled by a steep and deeply rooted fault, i.e. the Limpopo fault. We infer that strike-slip or slightly trans-tensional rifting occurred along the LM and was accommodated along this Limpopo fault. At depth we propose that ductile shearing was responsible for the thinning of the continental crust and an oceanward flow of lower crustal material. This process was accompanied by intense magmatism that extruded to form the volcanic basement and gave to the corridor its peculiar structure and mixed nature. The whole region remained at a relative high level during the rifting period and a shallow marine environment dominated the pre-Neocomien period during the early phase of continent-ocean interaction. It is only some times after break-up in the MB and the initiation of the MFZ that decoupling occurred between the MCP/NNV and the corridor allowing for the latter to subside and being covered by deep marine sediments. A scenario for the early evolution and formation of the LM is proposed taking into account both recent kinematic and geological constraints. It implies that no or little changes in extensional direction occurred between the intra-continental rifting and subsequent phase of continent-ocean interaction.

1 Introduction

25 East-Gondwana break-up led to the separation of four independent continental blocks, namely Africa, Antarctica-Australia, Madagascar-India and Patagonia. This fragmentation strongly segmented the East-African margins in a succession of divergent and strike-slip segments (Figure 1). To the north, southward motion of the Madagascar-India plate along the Davie Fracture Zone (DFZ) opened the Somali Basin (SB). Similarly, the Antarctica-Australia plate drifted southward with respect to Africa along the Mozambique Fracture Zone (MFZ) and opened the Mozambique Basin (MB). Finally, further south-west, the Patagonia plate escaped from the coast of South-Africa along the Agulhas-Falklands Fracture Zone (AFFZ) while seafloor spreading occurred in the South Natal Valley (SNV).

The exact timing and mechanisms of Gondwana break-up remain, however, still speculative. Namely, the Mozambique Coastal Plain (MCP) in southern Mozambique and its offshore prolongation the North Natal Valley (NNV) form a wide buffer zone inherited from this complex break-up (Figures 1 and 2). It is surrounded to the north and west by the Lebombo and Mateke-Sabi monoclines representing continental flood basalts (CFB) and associated dike swarms of Lower-Jurassic Karoo age (e.g., Jourdan et al., 2005; Watkeys, 2002) and, to the south and east, by oceanic crust of the MB and SNV respectively of Upper-Jurassic (e.g., Mueller and Jokat, 2019) and Lower-Cretaceous (Goodlad et al., 1982) ages. In the absence of modern deep seismic investigation, the crustal nature of the area is highly debated. Many have interpreted the presence of thickened oceanic crust and/or thinned continental crust with high magmatic content based on scarce seismic data, potential field data, and/or geological correlation with the conjugate margin in Antarctica's Western Dronning Maud Land (DML) (e.g., Klausen, 2009; Leinweber and Jokat, 2011; Tikku et al., 2002; Watts, 2001). Consequently plate kinematic framework including so called 'tight' fit reconstruction have been privileged, where the DML overlaps fully or partly the MCP/NNV, and an initial phase of rifting oblique or normal to the subsequent southward plate drift is inferred (e.g., Martin and Hartnady, 1986; Cox, 1992; Klausen, 2009; Mueller and Jokat, 2019).

45 To shed new lights on the East-African margins structure and their formation processes the PAMELA (PAssive Margins Exploration Laboratories) project was initiated in the early 2010th by TOTAL and IFREMER in collaboration with French universities (Université de Bretagne Occidentale, Université Rennes 1, Université Pierre and Marie Curie), the CNRS and the IFPEN. In 2016, the PAMELA MOZ3-5 cruise acquired seven combined multi-channels and wide-angle seismic profiles in the MCP/NNV area (Moulin and Aslanian, 2016; Moulin and Evain, 2016) (Figure 2). Velocity models built from these data challenge the 'tight' fit scenario as they unravel the continuity of a thick and highly intruded continental crust beneath the MCP and NNV (Moulin et al., 2020; Lepître et al., 2021; Watremez et al.). Conversely these results strengthen previous studies that interpreted continental crust in the area (Domingues et al., 2016; Hanyu et al., 2017) and brings strong support for a 'loose' fit plate reconstruction without plates overlap (Thompson et al., 2019). Within such framework, both rifting and subsequent spreading are inferred to proceed from a continuous quasi N-S movement of Antarctica-Australia and Madagascar-

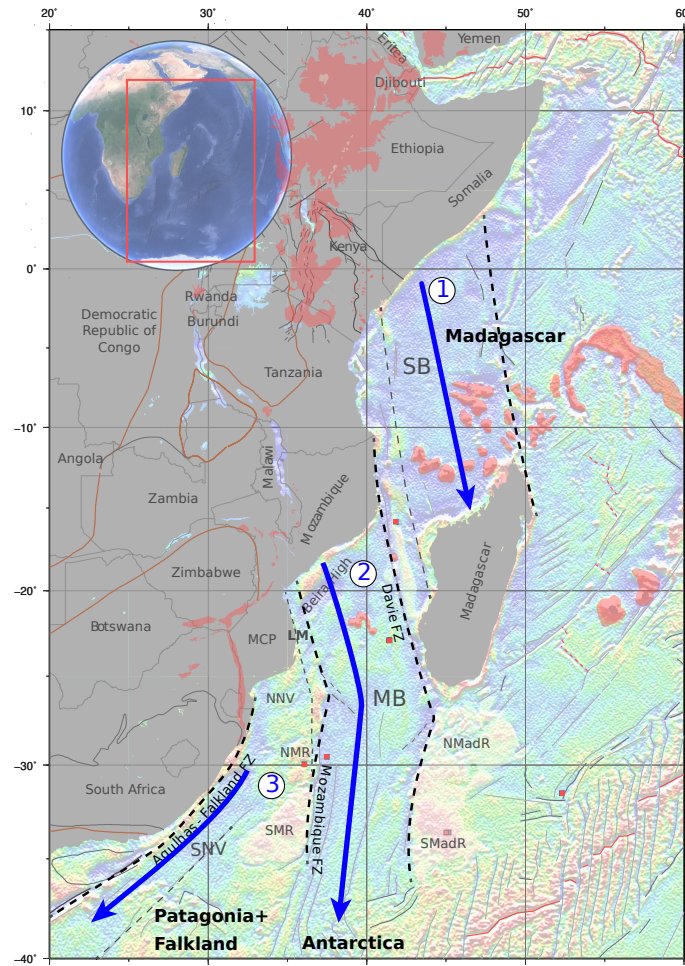


Figure 1. Free-air satellite-derived gravity anomaly of the Mozambique Channel (Sandwell et al., 2014) showing the complexity and segmentation of the East African margin (modified from Thompson et al. (2019)). Segments 1 and 2 correspond respectively to the movement of the Madagascar and Antarctica tectonic plates that opened the Somalie Basin (SB) and the Mozambique Basin (MB). The segment 3 corresponds to the drifting of the Falkland and Patagonian plates that opened the South Natal Valley (SNV). NNV=North Natal Valley; MCP=Mozambique Coastal Plain; NMR=North Mozambique Ridge; SMR=South Mozambique Ridge; NMadR=North Madagascar Ridge; SMadR=South Madagascar Ridge. Our study area is the Limpopo margin (LM, in bold). In red is volcanism without distinction about the age; black lines are major tectonic features; and brown lines denote craton contours (Mercator projection).

55 India plates with respect to Africa with major implication on the dynamics of rifting along the East-African margins and the age of Gondwana break-up.

To further constrain the Gondwana break-up, this study focuses on the MZ3 profile acquired during the PAMELA MOZ3-5 experiment (Figure 2). It investigates how rifting occurred to the east of the MCP/NNV along the Limpopo margin (LM), one of the East-African strike-slip segments. We produce both a p-wave velocity model of the sedimentary and deep crustal

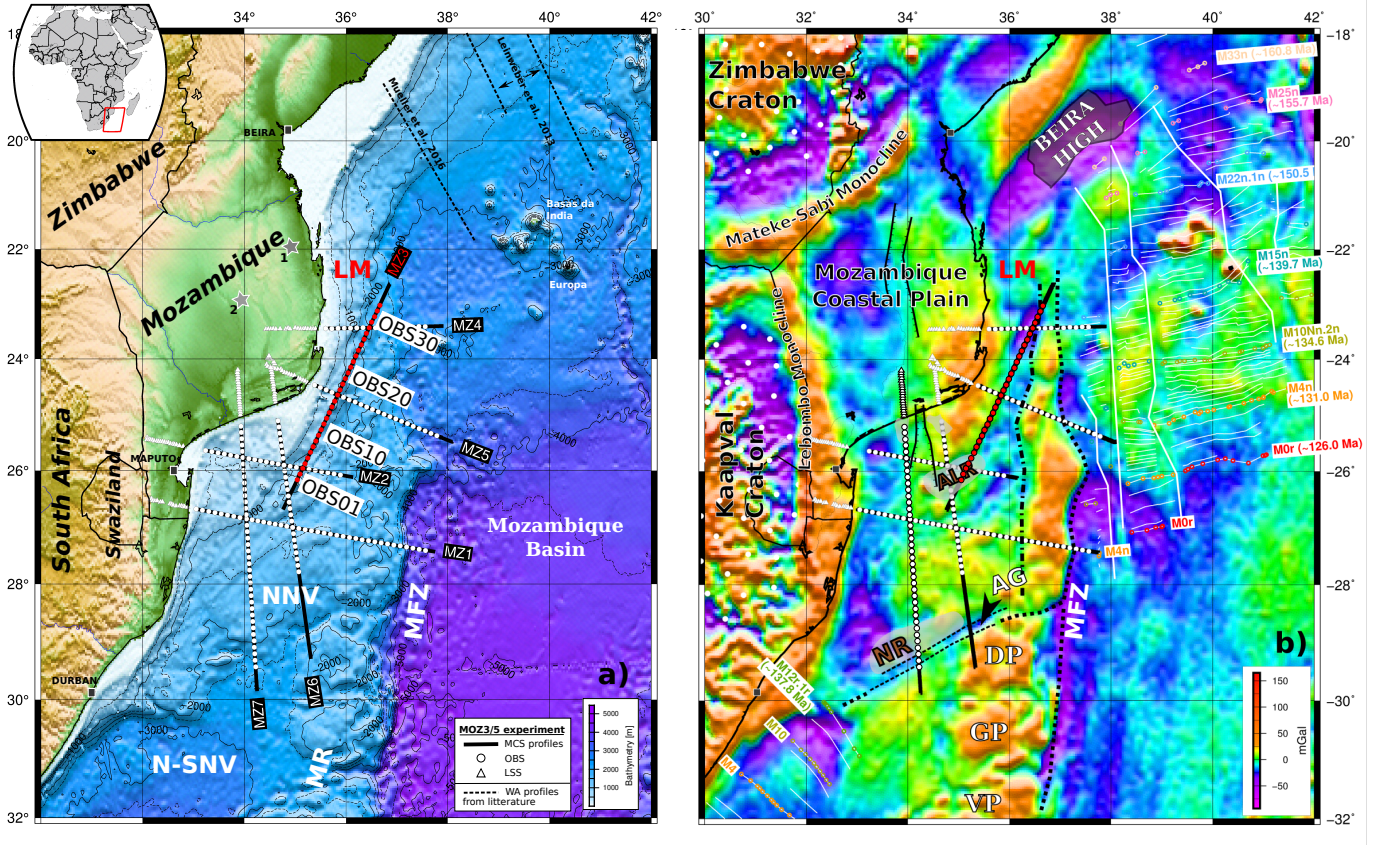


Figure 2. Maps of the PAMELA MOZ35 seismic experiment. Combined MCS and wide-angle profiles are in black lines. MZ3 is highlighted with red dots marking positions of OBS. Instruments (OBS and Landstations) and names of other profiles are in white. a) Topography and bathymetric (Smith and Sandwell, 1997) with inset for location of studied area. The gray stars indicated the location points of 1D Vs-depth profiles from Domingues et al. (2016). LM: Limpopo margin in red; NNV: North Natal Valley, N-SNV: northern South Natal Valley; MR: Mozambique Ridge. b) Free-air gravity anomaly grid (Pavlis et al., 2012; Sandwell et al., 2014). Main features known in the area are from Mueller and Jokat (2019), which are based on Leinweber and Jokat (2012) and Mueller and Jokat (2017) for the magnetic spreading anomalies in the Mozambique Basin, and on Goodlad et al. (1982) for the magnetic anomalies in the South Natal Valley. The outline of the Naude Ridge (NR) is from Goodlad (1986). ALR: Almirante Leite Ridge; AG: Ariel Graben; DP: Dana Plateau; GP: Galathea Plateau; VP: Vauban Plateau.

60 structure along the profile and a tectono-stratigraphic analysis of the area based on key industrial seismic lines. Our results are interpreted jointly with models from companion profiles to reveal the peculiarities of this margin and propose a scenario for its formation and early evolution within tight kinematic constraints.

2 Geological setting and controversies

East Gondwana break-up initiated on a heterogeneous lithosphere that was last reworked and assembled during the PanAfrican Orogeny about 720 to 550 Ma (Guiraud et al., 2005; Jacobs and Thomas, 2004). In southern Africa, PanAfrican structures include the Zambezi, Lurio and Mozambique belts. They linked together Archean and Proterozoic cratons (Zimbabwe and Kaapvaal) and belts (Limpopo, Namaqua-Natal) to their equivalents in Antarctica's Western Maud Land, namely the Grunehogna Craton and Maud Belt (Bingen et al., 2009; Jacobs et al., 2008; Riedel et al., 2013).

The Karoo sedimentary sequence and subsequent Karoo magmatism attest of widespread intercontinental tectonic and magmatic activities before Jurassic break-up. Karoo sediments consists of Late-Paleozoic to Early-Jurassic deposits within marginal basins in South Africa (Catuneanu, 2004) and interconnected rifts in Antarctica, Eastern Madagascar, and Central and East Africa (Daly et al., 1989; Elliot and Fleming, 2004; Geiger et al., 2004; Salman and Abdula, 1995). They were largely covered by Karoo continental flood basalts between 185 and 177 Ma while, up to 172 Ma, sills and dykes also massively intruded Precambrian basement structures in southern Africa and Antarctica's Dronning Maud Land (Cox, 1992; Hastie et al., 2014; Jourdan et al., 2007).

The MCP is known from industrial wells to be floored by volcanics but solid datations are lacking in support of a suspected Karoo age (Flores, 1973; Salman and Abdula, 1995). The oldest reliable age for basalts in the area concerns the Lower-Cretaceous Movene igneous that disconformably cover Karoo sediments to the east of the Lebombos monocline (Flores, 1973; Watkeys, 2002). As already stressed in companion papers (e.g. Moulin et al. (2020); Leprêtre et al. (2021)), the crustal nature in the area is the subject of a vigorous debate. The MCP gravity signature was previously interpreted as suggestive of oceanic crust (Watts, 2001) while continental crust was more recently favored based on ambient noise tomography (Domingues et al., 2016). Controversies also exist regarding the interpretation of weak magnetic anomalies within the NNV which could either sign fossil spreading centers (Green, 1972; Tikku et al., 2002; Martin and Hartnady, 1986; Leinweber and Jokat, 2011; Mueller and Jokat, 2019) or magmatic intrusions within a thinned continental crust (Hanyu et al., 2017). Available marine seismic data in the NNV and its conjugate margin were used in the past in support of either continental crust (Dingle and Scrutton, 1974; Lafourcade, 1984) or oceanic crust (Ludwig et al., 1968; Jokat et al., 2004; Green, 1972). With new deep seismic data acquired within the scope of the PAMELA project, companion papers of this study argue for continental crust below the MCP and NNV. Albeit its high magmatic content, Moulin et al. (2020) and Leprêtre et al. (2021) show the continuity of a thick crust with a comparable velocity structure than surrounding cratons and other continental structures worldwide.

Controversies further exist regarding the age of the first oceanic crust within the MB along the eastern MCP/NNV. It is generally considered to be around 155 Ma on both the Mozambique margin and its conjugate Riiser-Larsen Sea in Antarctica (Jokat et al., 2003; König and Jokat, 2010; Thompson et al., 2019). However, some studies reviewed the oldest magnetic anomalies found on the northeastern corner of the MB together with evidence of fracture zone paths on the gravity field to postulate an earlier initiation of seafloor spreading at 166-164 Ma (Leinweber and Jokat, 2012; Mueller and Jokat, 2019). This situation slightly differ on the opposite corner of the MB where early rifting concentrated in the offshore Zambezi depression before a rift jump isolated the Beira continental block from the rest of margin (Mahanjane, 2012; Mueller et al., 2016). Just

south of the Beira High (BH) the oldest magnetic anomaly identified is therefore dated at 155-157 Ma (Mueller and Jokat, 2019) (Figure 2).

100 In between, the interpretation of a clear N-S trending positive gravity anomaly is disputed. For many it is the natural prolongation of the MR oceanic plateaus located to the south (Figure 2). However, the tectono-stratigraphic study of Li et al. (2021) suggest here a volcano-sedimentary basement that formed during the intra-continental rifting period. In this case the MR would not extend further north but instead positive gravity anomalies would reflect the presence of large sedimentary features such as contourites as commonly observed in the area (Moulin et al., 2020; Thiéblemont et al., 2019).

105 All these elements have major implication regarding the location of the continent-ocean transition (COT). For Moulin et al. (2020), the SW-NE oriented Ariel Graben (AG) and Naude Ridge (NR) mark this COT. In 'tight' fit kinematic models, however, it is located just East and South of the Lebombo and Mateke-Sabi Monoclines respectively or slightly further inside the MCP (Martin and Hartnady, 1986; Klausen, 2009; Leinweber and Jokat, 2011; Mueller and Jokat, 2019). According to Mueller and Jokat (2019) the COT could also be located in the northern part of the NNV where several southwards ridge jumps may have occurred. Alternatively, Hanyu et al. (2017) divide the MR in a northern continental part, including the Dana and Galathea
110 plateaus, and a southern oceanic part including the Vauban plateau (Figure 2). This places the COT even further south than the AG and NR despite several studies that suggest the crustal structure and morphological characteristics of these plateaus formed in Lower-Cretaceous on a triple junction (Fischer et al., 2017; Gohl et al., 2011; König and Jokat, 2010; Leinweber and Jokat, 2012). It should be noticed, however, that some dredges made along the steep eastern border of the MR facing the MFZ and on its southwestern edge facing the SNV recovered Archean fragments of continental rocks and metamorphic samples of
115 African affinity (Ben-Avraham et al., 1995; Hartnady et al., 1992; Mougenot et al., 1986).

Following the formation of the southern Mozambique margins and MR intense post-rift tectonic activities reportedly affected the area. Long term subsidence is attested by the thick cover of Cretaceous to Neogene sediments over the MCP and NNV although this was perturbed by several tectono-volcanic events (Baby, 2017). Cenozoic to modern extension has also been emphasized within the MCP (Mougenot et al., 1986) and possibly southward in the NNV (Wiles et al., 2014). These days
120 extensional stress fields are reported in both Southern Africa and Madagascar (Adam and Lebedev, 2012; Piqué et al., 1999; Tsang-Hin-Sun et al., 2021) while there are increasing evidences for the southward propagation of the East-African rift system through both an onshore and an offshore branches (Mougenot et al., 1986; Deville et al., 2018; Courgeon et al., 2018). Those branches where recent volcanism concentrates possibly delineate actual micro-plates boundaries (e.g., Saria et al., 2014).

3 Combined Multichannel Seismic (MCS) and wide-angle seismic (WAS) acquisition, processing and modeling

125 3.1 Generalities

In 2016, the PAMELA MOZ3-5 cruises onboard french R/V Pourquoi Pas? acquired a total of seven coincident multi-channel and wide-angle seismic profiles over the southeastern MCP, the offshore NNV and LM (Figure 2; Moulin et al., 2020; Moulin and Aslanian, 2016; Moulin and Evain, 2016). This study concentrates on the 500 km long MZ3 profile trending SW-NE offshore the MCP. It runs from the NE edge of the NNV and crosses the LM towards the northwestern corner of the MB. To

130 illuminate the deep crustal structure thirty-two four-components Ocean Bottom Seismometers (OBS) from Ifremer's Marine Geosciences Unit were deployed every 7 nmi. 2960 shots were recorded by those instruments and by a 4.5 km, 720 channels, towed marine streamer. MZ3 crosses four out of the seven profiles acquired during the MOZ3-5 cruise: MZ2 and MZ6 (Schnürle et al., 2018) acquired over the NNV and, MZ4 and MZ5 that also crosses the LM (Watremez et al.). Two other profiles acquired in the NNV, MZ1 and MZ7 are presented by Moulin et al. (2020) and Leprêtre et al. (2021).

135 Ifremer's SolidQC software was initially used for processing MCS data. It allows data quality control, 2D geometry setup and SEG-Y file generation. Further processing was performed using CGG-Veritas Geocluster software. This sequence included external mute of direct and water wave arrivals, large band filtering (1-8-64-92 Hz), predictive deconvolution (440 ms operator, 252 ms IO, 32 ms gap), 4 ms resampling, seafloor multiple attenuation using Surface-Related Multiple Elimination (SRME) and RAMUR in the tau-p domain, time variant band-pass filtering, and pre-stack Kirchhoff migration. Velocity picking in
140 done after each major processing step in order to refine the final velocity model and build a coherent pre-stack Kirchhoff time migrated section (PSTM).

OBS WAS data processing included clock drift corrections, instruments localization using direct water wave arrivals to correct for the drift from their deployment position and eventually band-pass Butterworth filtering to improve travel time arrivals identification and picking.

145 We used the iterative procedure of two-dimensional forward ray-tracing followed by the damped least-squares travel-time inversion of the RAYINVR software (Zelt and Smith, 1992). Our modeling proceeded following a top-to-down strategy of arrival times fitting of both wide-angle reflected and refracted phases identified on OBS data. Starting from an initial velocity model including the bathymetry, model interfaces were inserted when a velocity change in apparent refracted velocity and a coincident high amplitude reflective phase were observed (i.e. phases triplication). Layers velocities and thickness were
150 adjusted in order to fit these phases. By converting our velocity model from depth to two-way travel time we checked and adjusted the geometry of the upper sedimentary and acoustic basement interfaces as identified on the MCS section (see Figure 3b).

Below we describe in details what guided our modeling by describing layers and their facies observed on the MCS line, then their corresponding refracted and reflected phases identified on OBS records. Overall combining MCS and WAS data we
155 identified four geological units along MZ3. From top to bottom they consist respectively of (a) the upper sedimentary package (orange/yellow Ps phases or interfaces in the following figures); (b) the volcano-sedimentary sequence that forms the acoustic basement on the MCS (green Psv phases or interfaces); (c) the crystalline basement (blue Pg phases or interfaces); and (d) the upper mantle (magenta Pn phases or interfaces). From MZ3 WAS data, this represents a total of 72750 picked arrival times that are summarized in appendix tables A1. Travel-time uncertainty for each phase was automatically calculated based on traces
160 signal to noise ratio. They range from 0.025 s for high ratio to 0.25 s for poor ratio.

3.2 MZ3 MCS line

MZ3 PSTM is shown in figure 3. The first hundred kilometers of MZ3 profile run over the NNV and are dominated by volcanic edifices of the Almirante Leite Ridge (ALR) which completely masks the underlying structure (-20 and 40 km). On each side of

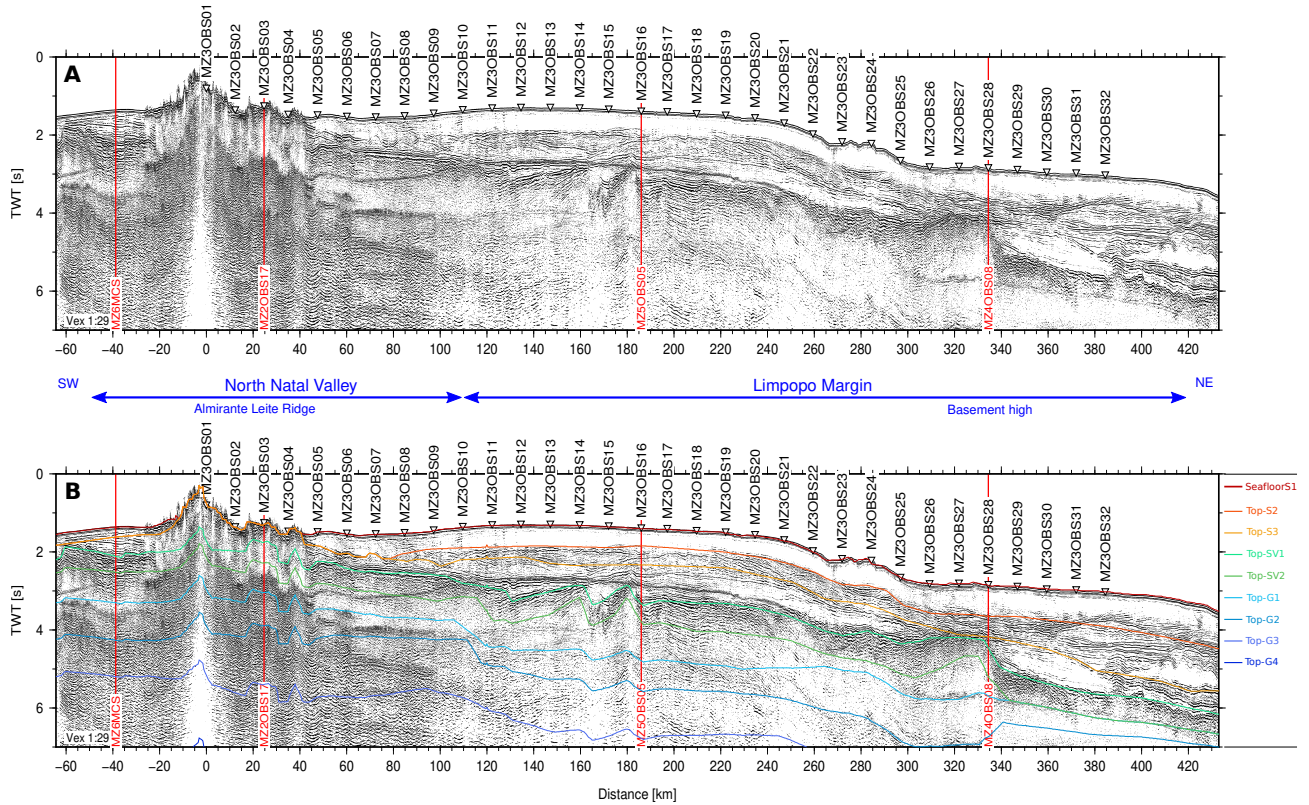


Figure 3. (a) Two-way travel-time record section of MCS data along MZ3 profile. (b) Same as (a) overlain by time converted interfaces from coincident wide-angle velocity model. Intersections with other profile from MOZ35 cruise are indicated by red line. OBS locations are indicated by inverted triangles.

the blind zone, a maximum of 1 s.twt of upper sediments is present. These consist of a first layer (S1) of weak signal and poorly resolved horizons below the seafloor. It is very thin to the SW of the ALR but thickens on its opposite side. At the bottom of S1 a stronger reflector (top-S3) is flat and parallel to the seafloor on the SW of the ALR but is dipping and undulating towards the NE. A few strong amplitude and unconformable reflections exist on each side of the ALR beneath this interface. A set of more continuous and coherent horizons marks the top of acoustic basement (top-SV1) which appears highly and steeply fractured to the SW of the ALR. At least 0.5 s.twt of parallel layering can be identified within the upper basement (SV1) on this side while more chaotic and incoherent signal dominates on the NE side of the ALR. Because energy is lost below about 3 s.twt the SV2 and deeper layers are constrained by OBS data.

With increasing model distance, the seafloor over the LM forms a slight dome between 120 and 260 km and then continuously deepens. S1 continues from the NNV as a 0.5 s.twt thick layer which internal structure is almost transparent because it is poorly resolved by our seismic. Below, S2 is a layer of intense but highly disrupted reflectivity revealing various sedimentary features, possibly channel incisions (100km model distance), contourites (360-400 km) and mass transport deposits (400-430

km). This contrasts with the S3 layer where more continuous and organized horizons are present, though of weaker amplitude. The top of the acoustic basement (top SV1) corresponds to a set of parallel and stronger amplitude reflectors in continuity with the NNV up to 300 km model distance. There a transition to a rugged surface marked by a broad basement high occurs. To the SW of the high the basement internal structure (SV1) shows clear parallel or dipping reflectors while to its NE it is chaotic with incoherent signal. There are two trends in dipping reflectors: one to the NE slowly dipping toward the western edge of the basement high (240-260 km) and a second, dipping to the SW, that coincide with highly fractured and sharp basement. Only the internal structure of the SV1 layer, about 0.5 s.twt thick, is imaged by the MCS. No energy reflects further down and, SV2, crystalline basement (G1-G4), the Moho (top-Moho on figure 3b) are constrained from wide-angle seismic only.

3.3 MZ3 WAS data

We selected key OBS sections to illustrate this section but all records can be found in Supplementary Materials with their corresponding synthetic sections, travel times picks and fits, ray-tracing through the final model and the coincident portion of MCS line.

On most OBS records, 2 or 3 refracted and associated reflected phases describe the sedimentary package (e.g. orange phases on figures 4A-4D). Those refracted phases have apparent velocities and offsets rarely exceeding 3 km/s and 20 km respectively. They are visible as first arrivals at very short offsets then generally extend as secondary arrivals. Corresponding reflected phases are generally well observed at short offsets inside the cone formed by direct wave arrivals (red phase). Their travel times are coherent with those of the main horizons seen on the MCS profile (top-S2 and top-S3 on Figure 3b). Clear examples of sedimentary phases can be observed on MZ3OBS14 and MZ3OBS30 record sections (Figures 4B and 4D) located on the LM. Sedimentary phases recorded on instruments located on top or near the ALR are highly heterogeneous. The velocity structure is difficult to model and thus poorly constrained. As shown on MZ3OBS03 (Figure 4A) there are high apparent velocities at short offsets followed by a shadow area. This is modeled by a negative velocity contrast reflecting the presence of high velocity extruded volcanic material on top of lower velocity sediments.

The top of the acoustic basement is marked on OBS records by a strong amplitude reflected phase (green Top-SV1), generally the latest visible within the water cone which correlates well with observations made on MCS (Figure 3b). The amplitude contrast is created by a strong velocity jump of at least 1.5 km/s. Instruments located over the NNV and the LM west of the basement high indicates the presence of two layers within the acoustic basement. There is a first set of associated refracted/reflected phases (SV1) with apparent velocities lower than 5 km/s and a second set (SV2) with velocities higher than 5 km/s. (e.g. MZ3OBS20 on figure 4C). The first of these layers when converted to two-way-time coincides with the deep layering previously described on MCS (SV1 layer on Figure 3b). However, its base and the SV2 layer below are entirely constrained by wide-angle data. To the NE of the basement high, OBS evidence a clear change in the characteristics of the acoustic basement internal structure as already suggested from its facies on MCS. Here a single layer (SV1) continues while SV2 is absent below the basement high. Apparent velocities are between 5 and 5.5 km/s (e.g. MZ3OBS30 on figure 4D) which are intermediate between those of SV1 and SV2 beneath the NNV and LM. Therefore, despite its prolongation toward the northeastern end of the line, the basement high appears as a clear marker of a change in nature of the acoustic basement.

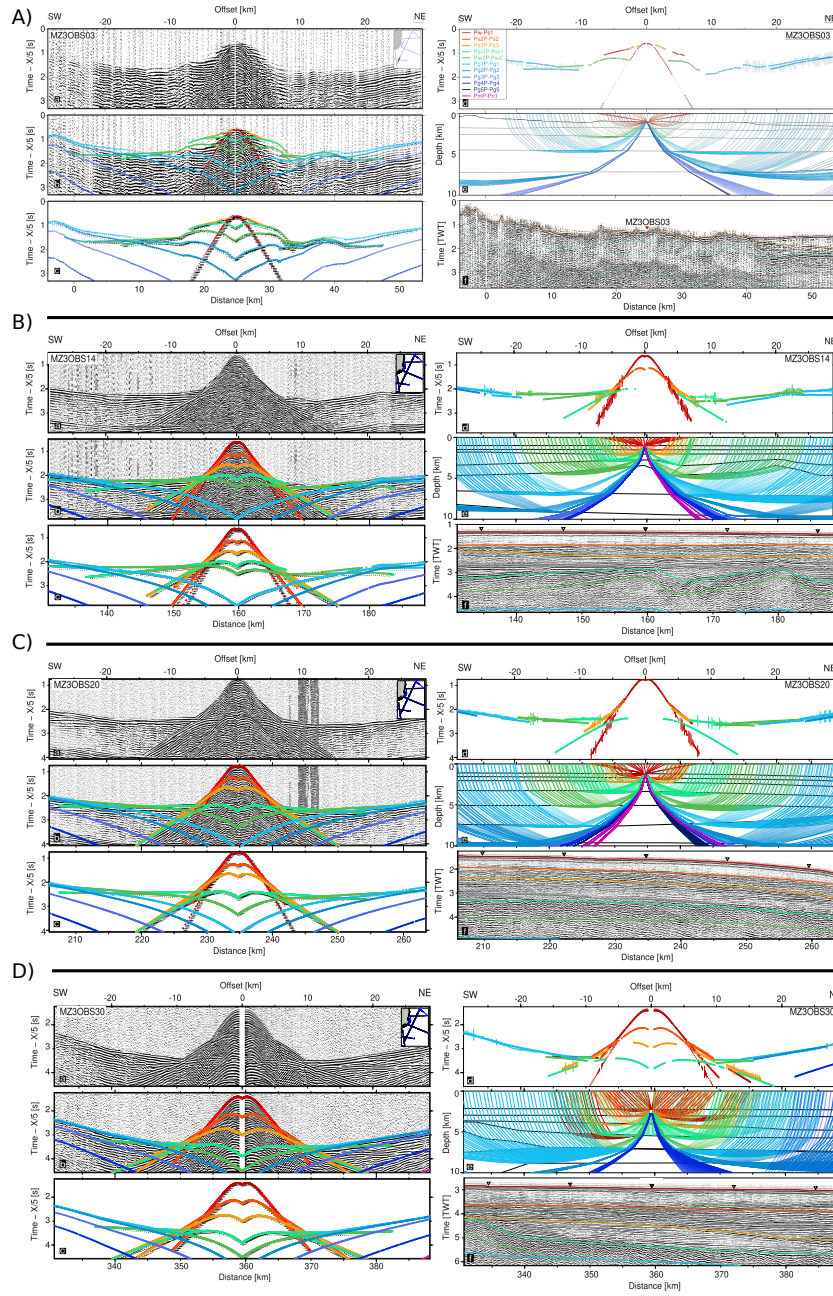


Figure 4. Sedimentary and volcano-sedimentary seismic phases on A) MZ3OBS03, B) MZ3OBS14, C) MZ3OBS20, D) MZ3OBS30. For each instrument 6 panels display a) seismic record; b) seismic record with color-coded predicted arrivals; c) synthetic section with color-coded predicted arrivals; d) color-coded picked travel-times with uncertainty bars overlain by dotted predicted times; e) color-coded seismic rays; f) MCS time migrated section with color-coded model interfaces. On a, b, c, and d, travel-time is reduced by a velocity of 5 km/s.

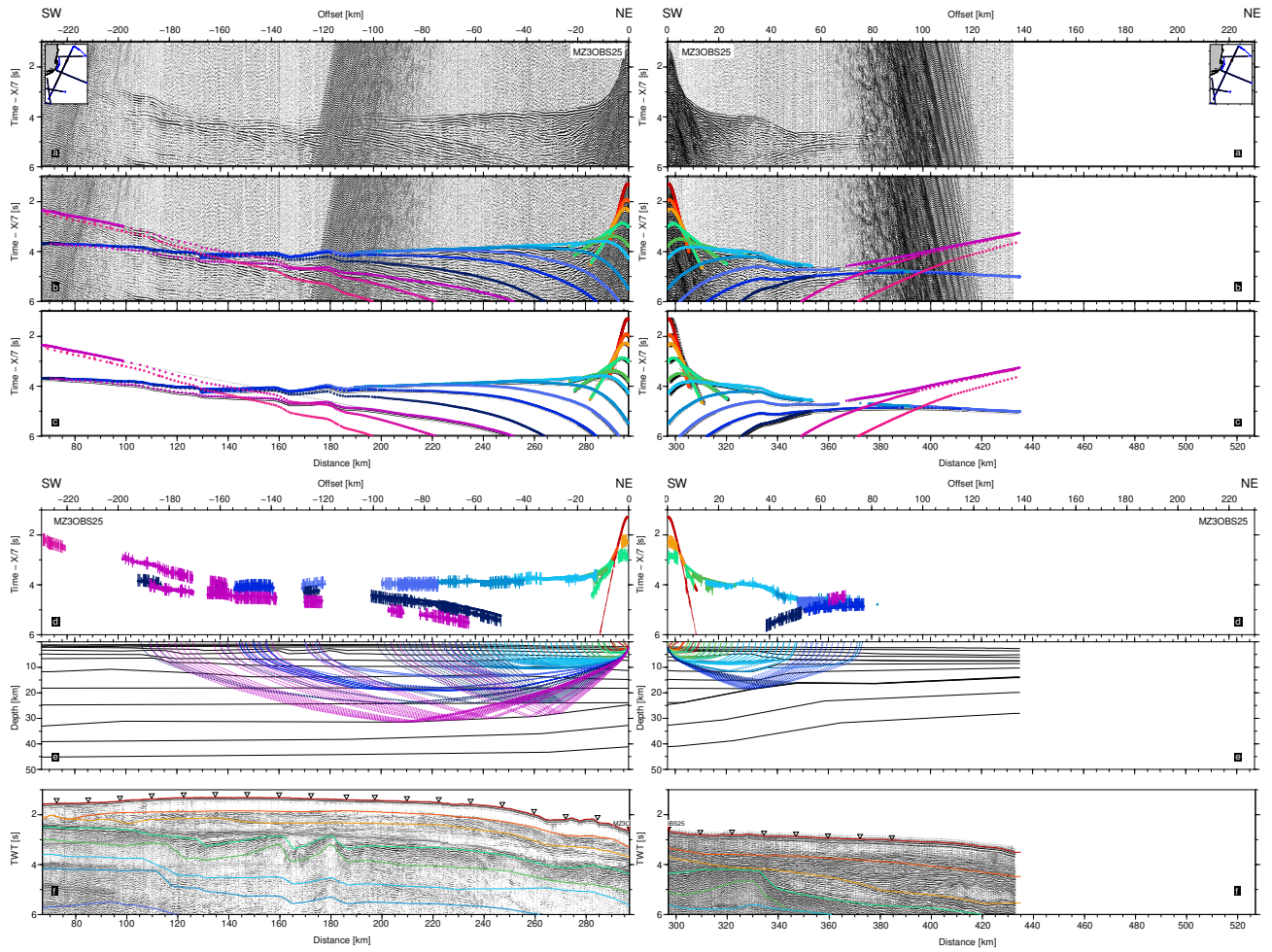


Figure 5. Seismic phases from the crust and mantle on MZ3OBS25. Left panels represent negative offsets (toward the SW) and right panels positive offsets (toward the NE). On each side 6 panels display a) Seismic record; b) Seismic record with color-coded predicted arrivals; c) Synthetic section with color coded predicted arrivals; d) Color coded picked travel-times with uncertainty bars overlain by dotted predicted times; e) Color coded seismic rays; f) MCS time migrated section with color-coded model interfaces. On a, b, c, and d, travel-time is reduced by a velocity of 7 km/s.

210 The crystalline basement of the LM in the central portion of MZ3 is very well constrained by OBS records. They show long
 offsets refracted phases with only mild variations in apparent velocities (blue Pg phases). These are associated with numerous
 and quite high amplitude reflected phases (blue Top-Pg phases). These combined observations suggest a thick crust made
 characterized by a low velocity gradient but a strong internal reflectivity. At least 5 layers can be identified based on an average
 account of triplications between refracted and reflected phases. Apparent velocity of refracted phases ranges from 6.5 km/s
 215 for the shallow crust to 7 km/s or slightly above for the deep crust (e.g MZ3OBS11 and MZ3OBS25 on figures 5 and 6).

Triplication between crustal and mantle phases occurs typically at about 150 km offset. This offset decreases to less than 100 km for instruments located close to the NE end of the profile (e.g MZ3OBS31 on Figure 7) implying important crustal thinning.

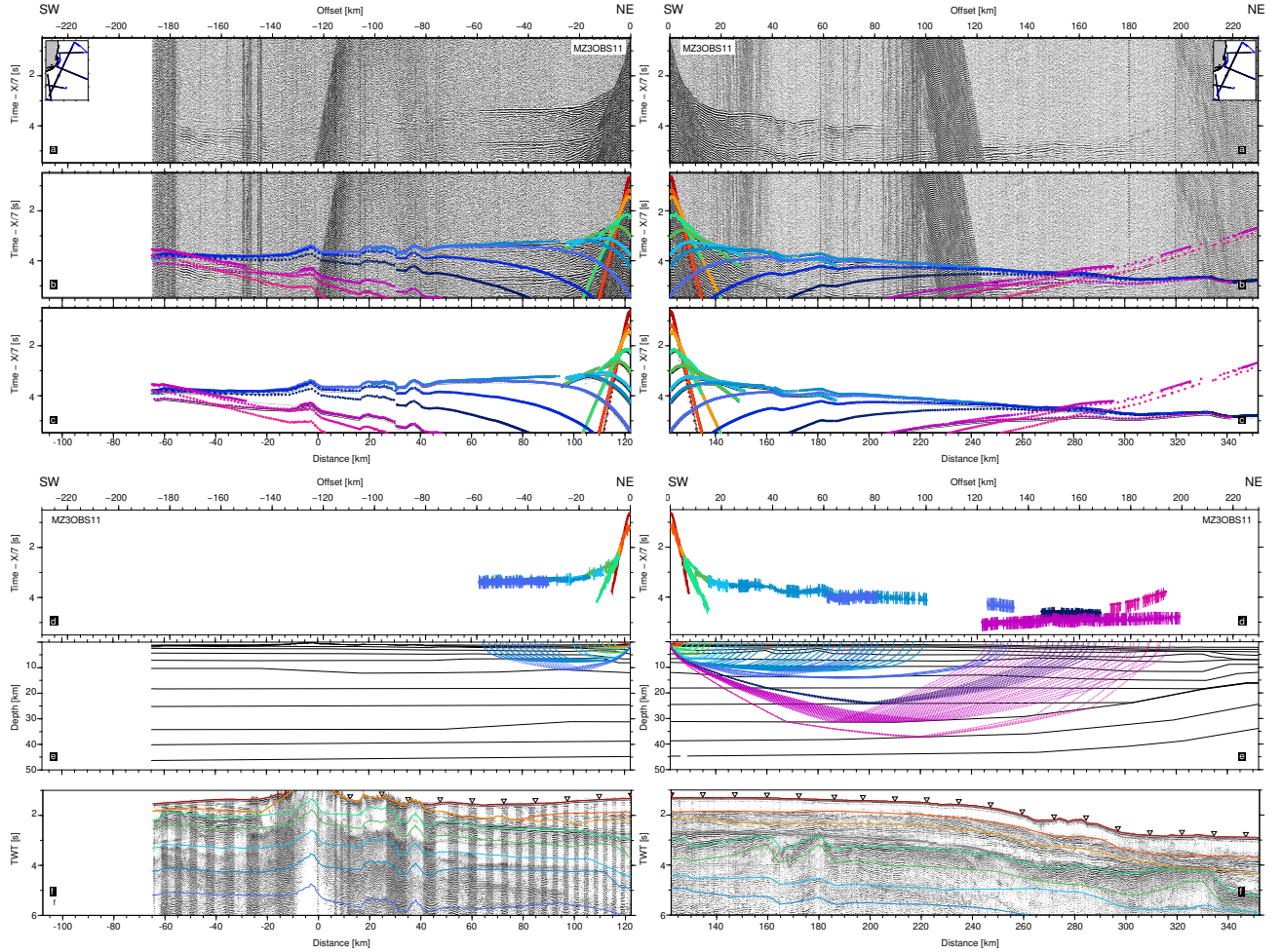


Figure 6. Same as figure 5 for MZ3OBS11

A different pattern of crustal phases is indeed observed on OBS records from the NE extremity of the LM. Crustal refracted phases at short offset suggest a stronger gradient and an average apparent velocity around 6.5 km/s. The gradient reduces at greater offsets but apparent velocities do not exceed 7 km/s. Some reflected phases can be distinguished but overall there is no more evidence for intense crustal layering, the most prominent corresponding to the Moho. The transition to mantle phases occurs at a relatively short offset (about 50 km on MZ3OBS31; Figure 7) suggesting thin crust. As for the acoustic basement, all these features combined depict a clear change in crustal nature.

The deep velocity structure beneath the NNV is only partly constrained because volcanism at the ALR creates seismic blind zone. Moreover, our acquisition geometry does not allow for optimal ray coverage beneath the edifice with OBS only located

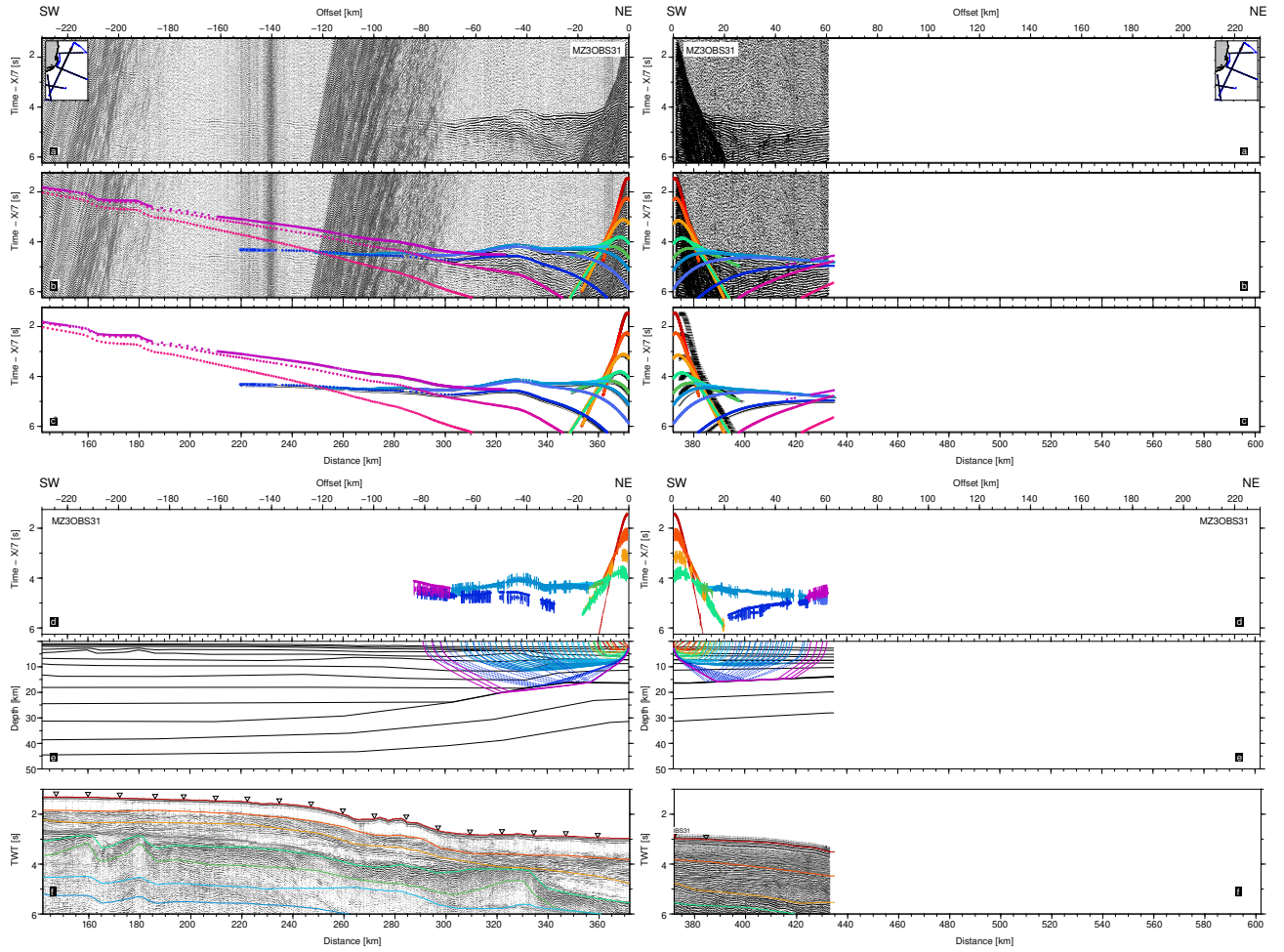


Figure 7. Same as figure 5 for MZ3OBS31

on top and to the NE of the ridge. Thus the two upper crustal layers of the model are only reasonably well resolved, with clear refracted and reflected arrivals of apparent velocities around 6 km/s and 6.5 km/s. The deeper crustal structure is poorly constrained (see MZ3OBS11 on figure 6). Though refracted phases cannot be identified, some higher amplitude phases can be distinguished at specific offsets ranges. Those can be explained as resulting from reflected waves from a layered medium similar to the one modeled for the LM. We can further interpret some far offset phases (e.g. MZ3OBS10 on figure 8) as reflection from the Moho if considering a depth of about 35 km for this interface as suggested by the modeling of the crossing MZ2 and MZ6 profiles (Schnürle et al., 2018) Nonetheless the poor constraints, we can reasonably consider the deep crustal structure beneath the NNV and ALR as similar to the western part of the LM up to the basement high. Our dataset reflect for both domains a thick crust with strong internal reflectivity, a low velocity gradient and high bottom velocities (7.3 km/s).

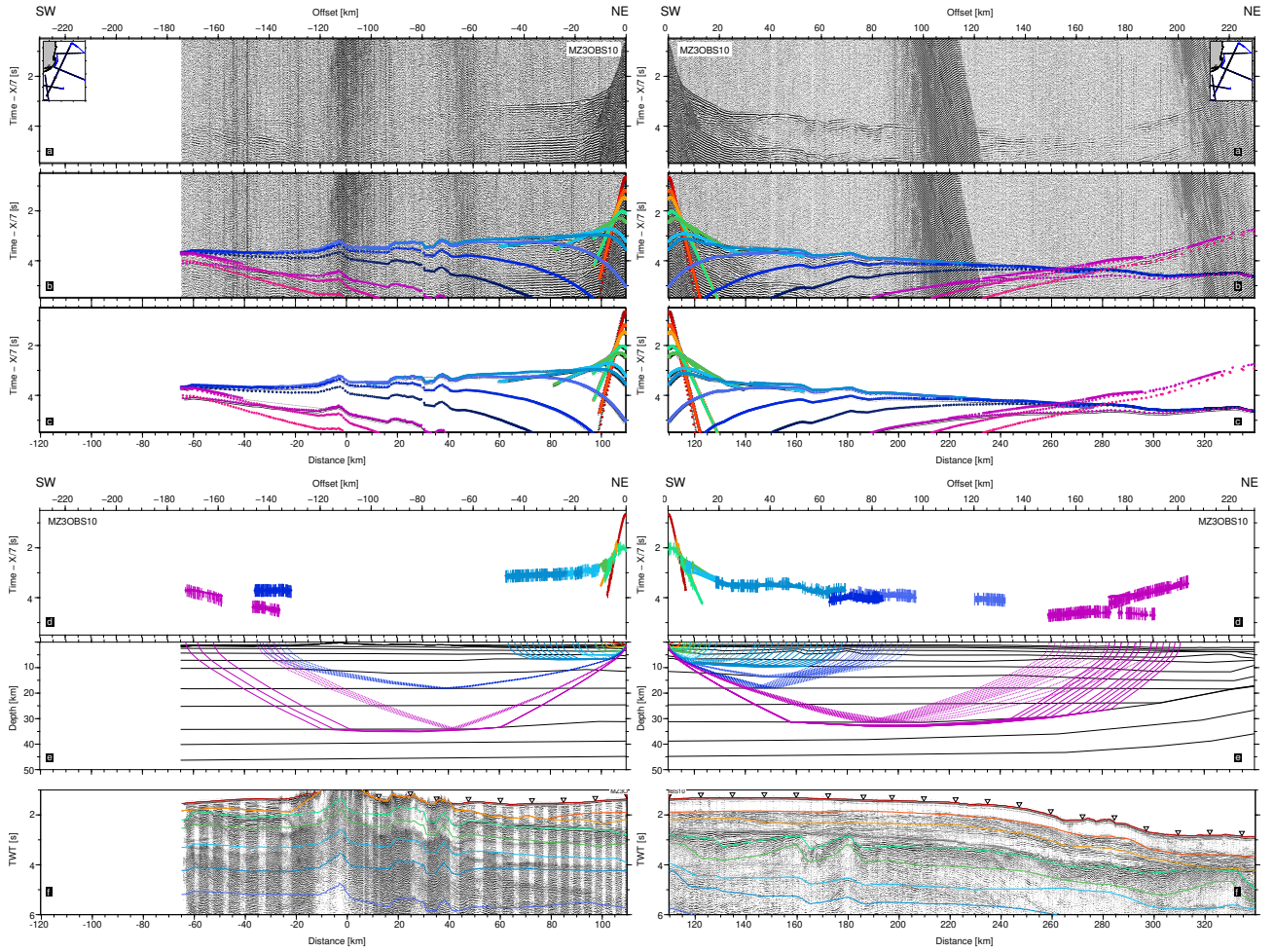


Figure 8. Same as figure 5 for MZ3OBS10

235 Arrivals from the mantle are observed on numerous OBS records throughout the profile. With many reflected phases con-
 verging towards the triplication point between crustal and mantle phases due to low velocity gradient within the crust, there
 is generally high amplitude signals at this place on OBS records, making the identification of the starting point of the mantle
 refracted phase difficult. The consequence might be some larger uncertainties on the depth of the Moho and uppermost mantle
 velocities. However, these can be balanced using constraints from crossing profile MZ2 (Schnürle et al., 2018), MZ4 and MZ5
 240 (Watremez et al.) which agree at a maximum of ± 2 km on the depth of the Moho. Refracted mantle phases show increasing
 apparent velocities from 8.0 to 8.3 towards the NE (Figures 5-8). Travel time fit for these phases is not perfect and uneven from
 one records to another which might also suggest important mantle heterogeneity along the profile. This heterogeneity is further
 evidenced by the presence of high amplitude mantle reflected phases on some records. Their dip are difficult to model with
 horizontal layering only. They may reveal local highly reflective body diffracting seismic waves. Anyhow, this suggest that the

245 heterogeneous and highly reflective character of the crystalline basement might continue downward within the mantle of NNV and western LM. Again we do not have evidence for such mantle reflectivity below the thin crust in the NE extremity of the LM but we lack of offset on these OBS records.

4 Model assessment

Our final model explains 89% (64900) of the events picked with a global RMS travel-time of 65 ms which given the uncertainty
250 assigned for each phase results in a normalized chi-squared of 0.65. Travel-time RMS and chi-squared values for each phase and each instrument are detailed in appendix tables A1 and A2 respectively. This section aims at presenting various elements that were used in order to validate our modeling and final velocity model. They include a resolution analysis, our model's gravity response and and its estimated depth and velocity uncertainties. Finally, a pre-stack depth migrated (PSDM) MCS section is also presented.

255 4.1 Model evaluation and resolution

Figure 9 presents four indicators on the quality of MZ3 velocity model based on wide-angle data only. Interface depth node spacing as well as velocity node spacing are indeed key to model the lateral variations of the seismic velocity with sufficient resolution, but without introducing complexity not required by the data. Note that the four indicators are not calculated for the upper sedimentary package and the top of SV1 as those layers are constrained by coincident MCS data. Their topography is
260 directly sample on the MCS profile while velocities are modeled from wide-angle phases.

Logically the density of velocity and depth nodes as well as the number of reflective segments are higher in the central part of the model and decreases towards its edges and with depth (Figure 9a). Indeed these regions of the model are less sampled by rays (Figure 9b) usually from a single direction and data quality is either poorer or degrade naturally with increasing offsets. Because the model parameterization have been adapted to these limitations MZ3 shows overall limited smearing (± 3 , Figure
265 9c) and very good resolution (above 0.9, Figure 12d). The quality of the modeling decreases at depth and towards model extremities. Resolution values remain, however, higher than 0.5 which are still considered acceptable. Greater smearing occurs essentially in the lower crust where only few refracted rays travel. Those have been difficult to identified on OBS records because many phases converge around to the triplication point with the PmP and Pn (see 'Wide-angle seismic data' section above).

270 4.2 Gravity modeling

We tested the gravity response of our final model against the measured and satellite-derived free-air gravity anomaly along the profile (Figure 10). A 2-D model consisting of homogeneous density blocks was constructed from the MZ3 final velocity model by converting P-wave velocities to densities according to (Ludwig et al., 1970) empirical function. The resulting density ranges from 1800 kg/m³ to 2400 kg/m³ in the upper sedimentary units, 2500-2600 kg/m³ in the volcano-sedimentary sequence, 2700
275 to 3000 kg/m³ in the crystalline basement while we tested mantle densities between 3100 to 3300 kg/m³. The model was

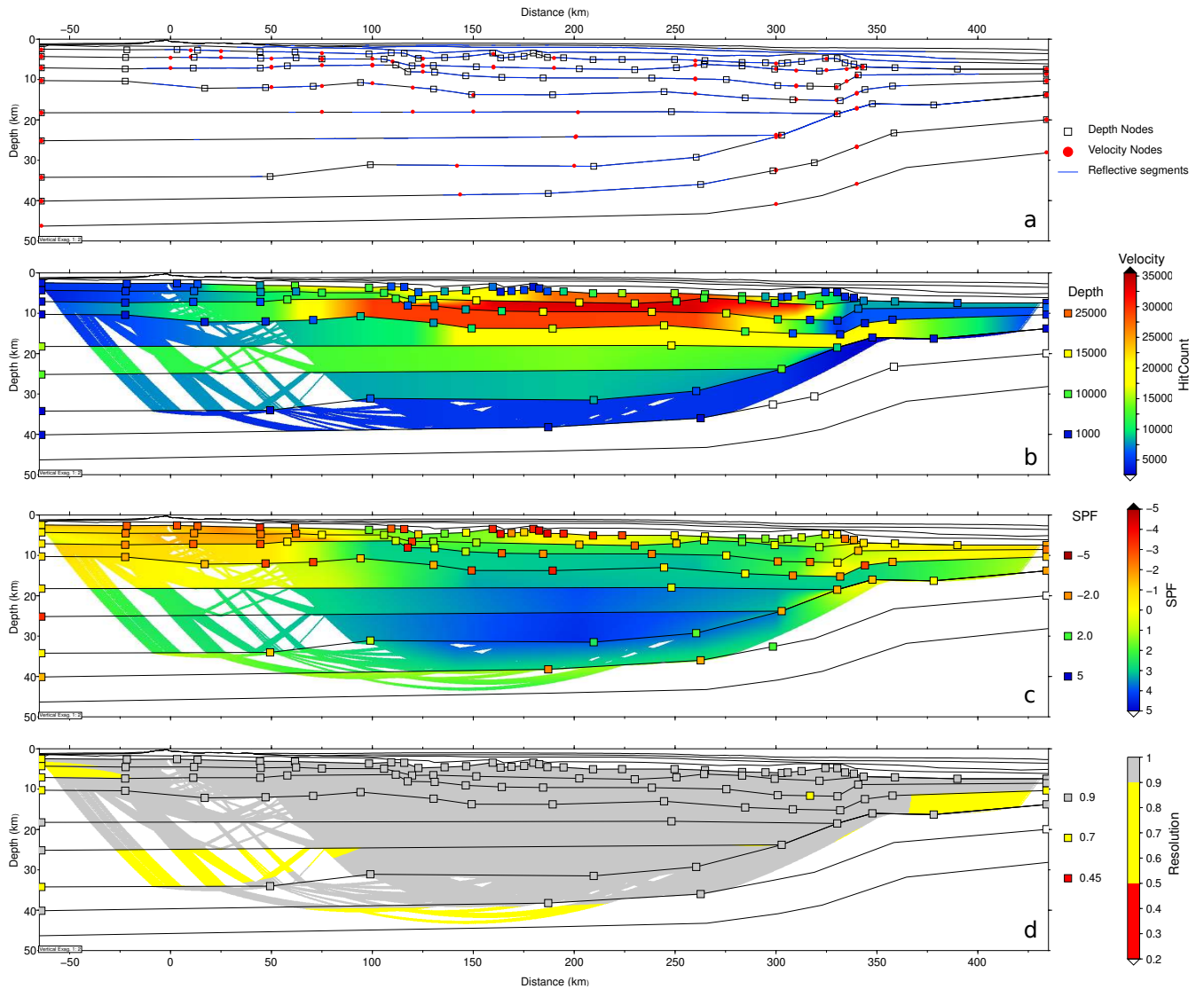


Figure 9. Evaluation of the wide-angle model MZ3. a) Model parameters including interface depth nodes (squares), top and bottom layer velocity nodes (red circles); interfaces where reflections have been observed on OBS data are highlighted in blue. b) Hit-count for velocity (colored) and depth nodes (squares). c) Smearing from Spread-Point Function (SPF) for velocity (colored) and depth nodes (squares). d) Resolution of velocity (colored) and depth nodes (squares). Zones that were not imaged are blanked.

extended down to 100 km where isostatic compensation may be reached, and 500 km laterally on each sides to avoid edge effects.

The gravity anomaly is relatively flat along and parallel to MZ3 profile and does not exceed ± 30 mGal (Figure 10b). There is sharp positive peak at the ALR and a broad negative one beneath the basement high of the LM which reflects the

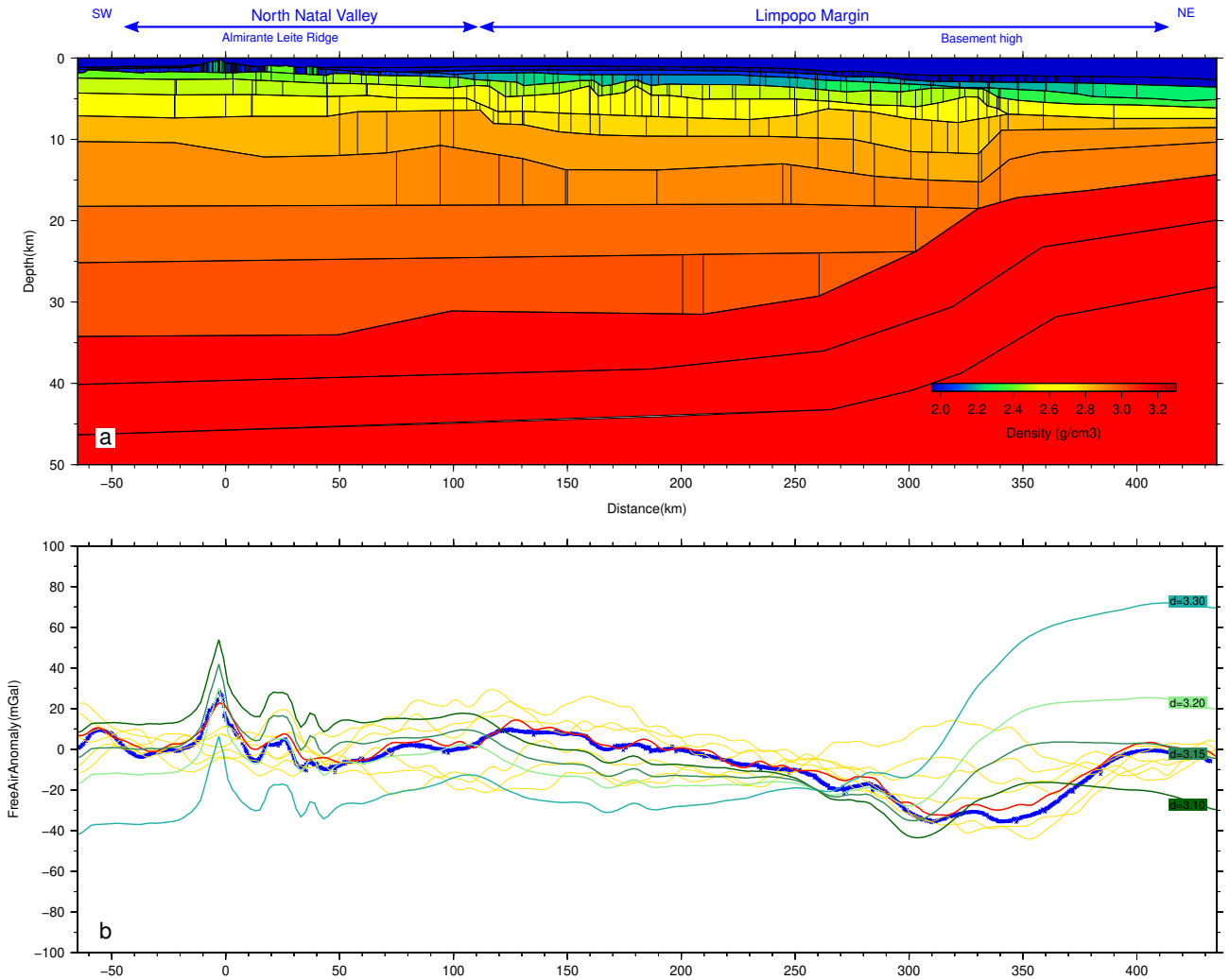


Figure 10. Gravity modeling along MZ3 profile. a) Density model showing blocks of equal density converted from the final velocity model according to (Ludwig et al., 1970) empirical function. b) Gravity anomaly along MZ3 profile. The free-air gravity anomaly derived from satellite altimetry (Pavlis et al., 2012) along the profile is in red while yellow curves correspond to similar profiles extracted at 10, 20 and 30 km laterally (yellow lines). The blue curve is the the gravity anomaly measured during the MOZ35 experiment. Green curves are calculated gravity anomaly from converted model in (a) according to several mantle densities (green labels).

280 change in crustal structure. Between these two peaks the lithosphere appears in isostatic equilibrium. The calculated gravity anomaly based on the conversion of MZ3 velocity model reflects the overall shape of the observed anomaly all along the profile. However, an acceptable fit can only be obtained by adjusting converted densities. This is achieved by lowering the density of the mantle layers from 3300 to 3150 kg/m³. Reduced mantle densities may signify the presence of a hotter than normal mantle. Besides or alternatively, this may indicate that the conversion of crustal velocities into densities are underestimated under the

285 NNV and western LM and vice versa at the NE extremity of the model. Our model does not generate a broad negative anomaly at the transition beneath the basement high of the LM but the change in crustal properties generates a clear jump from negative to positive values consistent we the observed gravity anomaly.

4.3 Uncertainties estimation

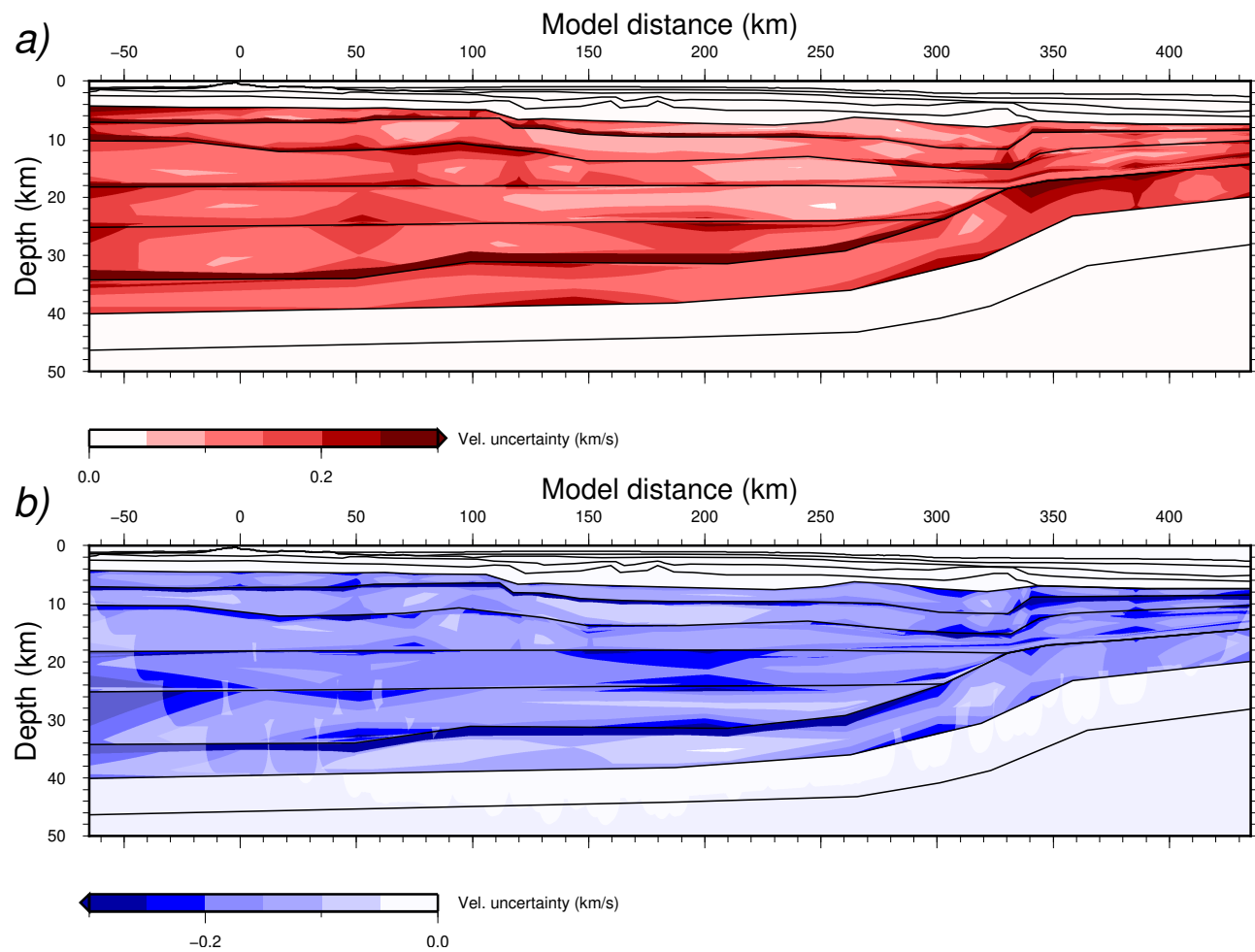


Figure 11. Global uncertainty plots for MZ3. a) Maximum and b) minimum admissible velocity deviations from the preferred model, built from 126 models within the thresholds defined in the text. Shaded areas indicate ray coverage. Preferred model’s interfaces are indicated by black lines and velocity deviations are colored according to color scales.

Velocity and depth uncertainties of MZ3 final velocity model were estimated using the Vmontecarlo code (Loureiro et al., 2016). Vmontecarlo explores the model space by generating random models. It evaluates the ability of each model to fit the observed data set and translate it to estimates of uncertainties given some quality thresholds.

For computational cost, the explored model space was reduced by limiting the number of parameters and fixing some bounds. For MZ3 we chose to maintain fixed sedimentary and volcano-sedimentary layers as well as basement depth nodes because those benefit from refined MCS constraints. This results in a total number of variable parameters of 148 as shown in figure B1.

295 We also allowed a maximum fluctuation of ± 0.50 km/s on velocity nodes while the maximum depth node variations were set to bands of 1, 2 and 3 km for the upper crustal, the 3 mid-crustal and the Moho interfaces respectively. We further limited the search by generating a maximum of 50000 random models and imposed a scaling factor for velocity and depth bounds that, starting at 20% of their maximum value, progressively increased to 100% within the first half of the randomly generated models. Finally the total number of observed travel times was decimated to be less than 50000 picks to reduced ray tracing

300 computing time.

Scores are calculated for each model according to a function that takes into account travel time fit and the ratio of traced rays to the number of observed events (Loureiro et al., 2016). MZ3 final velocity model gives a score of 0.88 with 43928 rays traced over the 49725 picks, an RMS of 0.07 s and, after adjusting the pick's uncertainties, a χ^2 of 1. Among the 50000 randomly generated models within the bounds given above, 46110 were valid and scored up to 0.81. Supplementary Materials give a

305 summary of this model space by plotting every 20 km model distance all 1D velocity-depth profiles color coded according to their normalized average score. Settings a confidence threshold at 95% of the maximum normalized average scores local depth uncertainties for a particular velocity can be estimated and vice versa. Vmontecarlo analysis shows that velocity uncertainties are globally stable around 0.1 km/s both along the model and with depth. Similarly, on average depth-uncertainties are quite stable along the profile. They increase with velocity from 0.5 km at 6.5 km/s to 1.5-2 km at 8 km/s. Higher uncertainties

310 values are observed around 300 km model distance because of the sharp transition in crustal structure and the potential lateral effects due to the orientation of MZ3. It is interesting to note that depth uncertainties for a velocity of 7 km/s is usually high over a couple of km to a maximum of 5 km in a few places. Up to 300 km model distance this can be explained by the very low velocity gradient required in mid/lower crust. In fact Vmontecarlo analysis further confirms that most of the basement is composed of material with velocities higher than 6.5 km/s even towards the NE end of the profile (distance greater than 320

315 km).

In order to visualize uncertainty estimates on profile a subset of possible alternative models were selected. These models respect the following criteria we judge acceptable: a score over 75% of the preferred model's score, a χ^2 lower than 2, a RMS lower than 0.1 s and at least 80% of the rays traced by the preferred model. This subset represents 126 models that were combined to produce the minimum and maximum admissible velocity deviations maps shown in figure 11. Large uncertainties

320 within the depth bounds allowed for interfaces are expected when large velocity contrast exist and should be ignored. Globally outside these hatched areas velocities can vary from ± 0.10 km/s to ± 0.15 km/s with rare excursions over ± 0.2 km/s.

4.4 MZ3 PSDM

A pre-stack depth migration and a residual moveout analysis were performed in order to convert MCS data from time to depth and verify the accuracy of the wide-angle velocity model. The Kirchhoff pre-stack depth migration procedure is described in

325 details by Schnürle et al. (2018) and the resulting section for MZ3 profile is shown in figure C1a. As for the pre-stack time

migration (figure 3) the full sedimentary cover is well imaged up to the top of the SV1 layer. Below, the section is mostly transparent with only intermittent and tiny events within the SV1 layer. In the common image gathers (CIGs: figure C1b), the top of Sv1 coincides with a strong low wavelength reflector, followed by poorly coherent and under migrated events. The semblance panels (figure C1c) is similarly well focused in the upper sediments and top of SV1 interfaces while it is blurred at greater depth and beneath the ALR.

5 Crustal structure of the Limpopo Margin

MZ3 final velocity model (Figure 12) consists of 13 layers beneath the seafloor: 3 for upper sediments (S1-S3), 2 for the volcano-sedimentary sequence (SV1-SV2), 5 for the crystalline basement (G1-G5) and 3 for the mantle (M1-M3). In this section we present the new constraints that the MZ3 MCS profile and velocity model bring on the crustal structure of the LM.

We further include results from a tectono-stratigraphy analysis we made along key industrial MCS profiles in the area and from the other velocity models built within the scope of the PAMELA project along adjacent profiles. This allows us to give an overview of the crustal structure of the LM from top to bottom including an interpretation of the stratigraphy of its upper sedimentary package, analyse the nature and deformation of its acoustic basement to finally focus on the crustal nature of the LM segments.

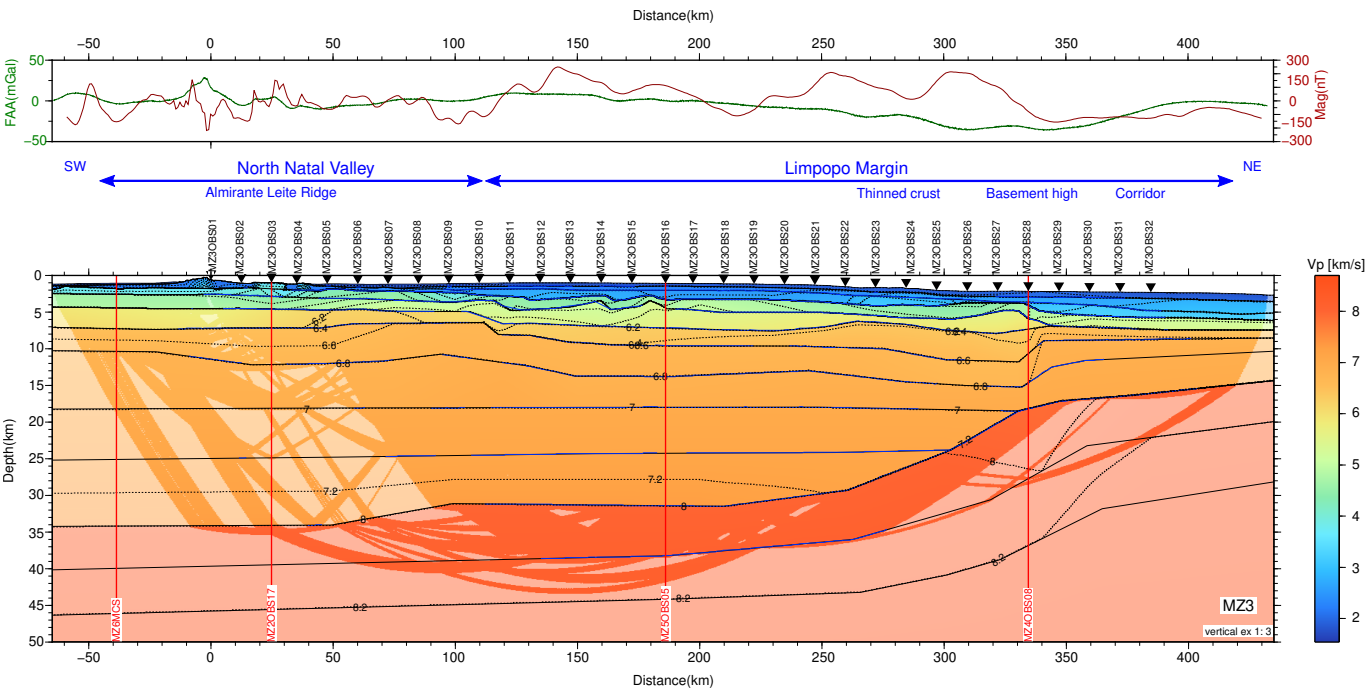


Figure 12. MZ3 Final P-wave velocity model with region constrained by seismic rays highlighted. Blue lines indicates where wide-angle reflections constrain the model interfaces otherwise in black lines. Inverted black triangles marks OBS positions. Vertical exaggeration is 1:3.

340 **5.1 Seismic stratigraphy of upper sediments**

Our final velocity model (Figure 12) shows two upper sedimentary layers over the NNV increasing to three layers over the LM (Figure 3). They are together less than a kilometer thick around the ALR and progressively thicken as the seafloor and acoustic basement deepens toward the NE. This package shows globally low velocities between 2 and 3 km/s top to bottom, reaching values slightly above 3 km/s at the northeastern end of the line where it is the thickest (3.5 km). It is therefore largely
345 made of uncompacted terrigenous sediments except close to the ALR where strong velocity contrasts and inversions suggest interleaved volcanic layers. Over the LM, sedimentary horizons are strongly deformed showing typical features of a margin shelf and slope with incised valley or reworked sediments such as mass transport deposits and contourites (Figures 3, 13).

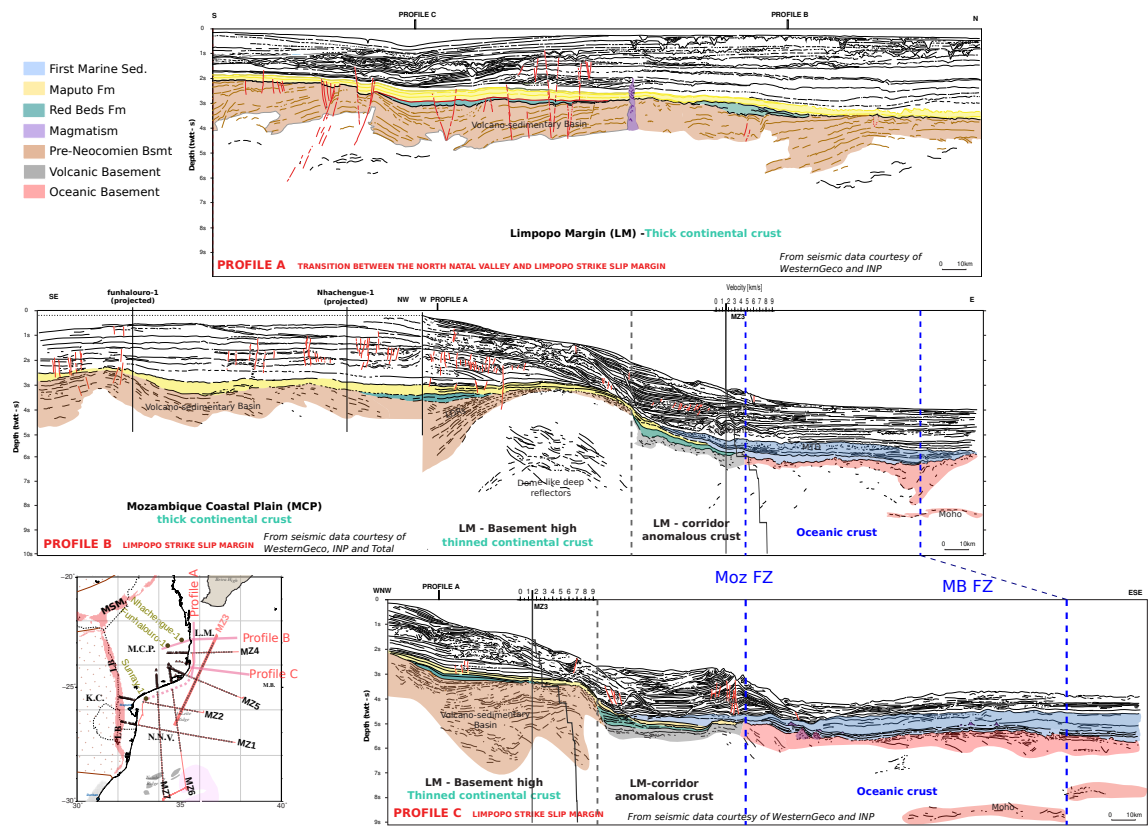


Figure 13. Compilation of line drawing of commercial MCS two-way travel-time profiles superimposed by stratigraphic interpretation. The map to the bottom left corner gives locations of these profiles with respect to seismic profiles acquired during the PAMELA MOZ3-5 cruise. Also reported are drills locations that help to constrain ages of early sedimentary deposits. We also plotted velocity vs depth profiles at locations where profiles B and C cross the MZ3 velocity model.

On the southern MCP and offshore Mozambique, several wells were drilled into this upper sequence and up to the acoustic basement for some of them. Combined with commercial seismic profiles (Figure 13) we performed a seismo-stratigraphy

analysis to constrain the ages of the oldest deposits which span the syn-rift and early post-rift period that are of interest for this study. More precisely we extended to the LM previous seismo-stratigraphy studies produced for the NNV (Baby et al., 2018; Schnürle et al., 2018). Profile A is the direct north-south prolongation along the LM of a profile presented by these authors. It connects to the Sunray 1 well (Salman and Abdula, 1995) located in the NW corner of the NNV (Figure 13). We further analyzed two profiles (B and C) than are normal to profile A and strike roughly E-W across the LM. Among them Profile B has an onshore portion that connects to Funhalouro-1 and Nhachengue-1 wells and Line SM-59 presented by Salman and Abdula (1995). Along all these lines, the horizons of late-Jurassic to Neocomian formations, namely Red Beds Fm and Maputo Fm (in green and yellow respectively on figure 13), can be confidently extended towards the LM from both the NNV (Sunray-1 well) and the MCP (Funhalouro-1 and Nhachengue-1 wells). As mentioned by Salman and Abdula (1995), these two formation unconformably cover the acoustic basement. Red Beds are only observed filling local fossil depressions on the MCP and northern NNV (Figure 13, green deposits). A possible similar deposit is interpreted at the eastern foot of the basement high on Profiles B and C. On top of these restricted deposits or directly on the acoustic basement, the Maputo Fm appears widespread over both the NNV and the MCP. Most importantly, a continuous sequence of Maputo Fm (in yellow), akin strongly eroded, can be drawn on Profile B across the entire LM. It indeed passes clearly over to the east of the basement high where the first marine sediments (in blue on figure 13) are seen onlapping the formation. This constrains the age of the LM acoustic basement in pre-Neocomien time and before the onset of seafloor spreading on the MB.

5.2 Nature and deformation of the acoustic basement

At the base of upper sediments, the top of the acoustic basement as identified on MZ3 MCS line consists of a set of high amplitude parallel reflectors over the NNV and western LM changing to a rough surface to the NE end of the line (top of SV1 on Figures 3). On the velocity model (Figure 12), it is characterized by a large velocity jump (1-1.5 km/s) to reach velocities of 4.5-5 km/s. It is relatively flat over the NNV at about 2 km depth and deepens from 3.5-4 km in the LM to 6 km passed 330 km model distance. Its perturbed topography evidences important deformations most probably controlled by highly dipping and near vertical faults. On each side of the ALR they bound a few horsts and grabens while over the LM they are highlighted by fan-like dipping reflectors and steep basement highs. The most prominent basement high, located at 310-340 km model distance, is clearly an isolated basement structure controlled on each side by steep faults. To its SW, the fault zone appears wider at the basement surface suggesting a deep fault rising as a flower system (Figure 3).

Internally the acoustic basement show chaotic and incoherent signal in some places (60-120 km, 300-420 km, Figure 3) but also clear basement-parallel or dipping reflectors of variable amplitude in others (-60 to -20 km; 120-260 km). This mixed nature already suggests that the top of the acoustic basement is not the roof of the crystalline basement, at least up to the basement high at 330 km where it is more homogeneous. Its internal structure is, however, only partially resolved by the MCS. WAS data further constrain a continuous, 3 to 4 km thick, unit made of two layers (SV1 and SV2 layers in green on figure 3b). They are respectively 1-1.5 km and 1-2.5 km thick with velocities ranges of 4-5 km/s and 5-6 km/s on average though slightly lower values are observed beneath the ALR (Figure 12). From its seismic facies and velocities we therefore argue for the presence of a deep volcano-sedimentary unit that is continuous from the NNV towards the LM. This unit possibly ends at

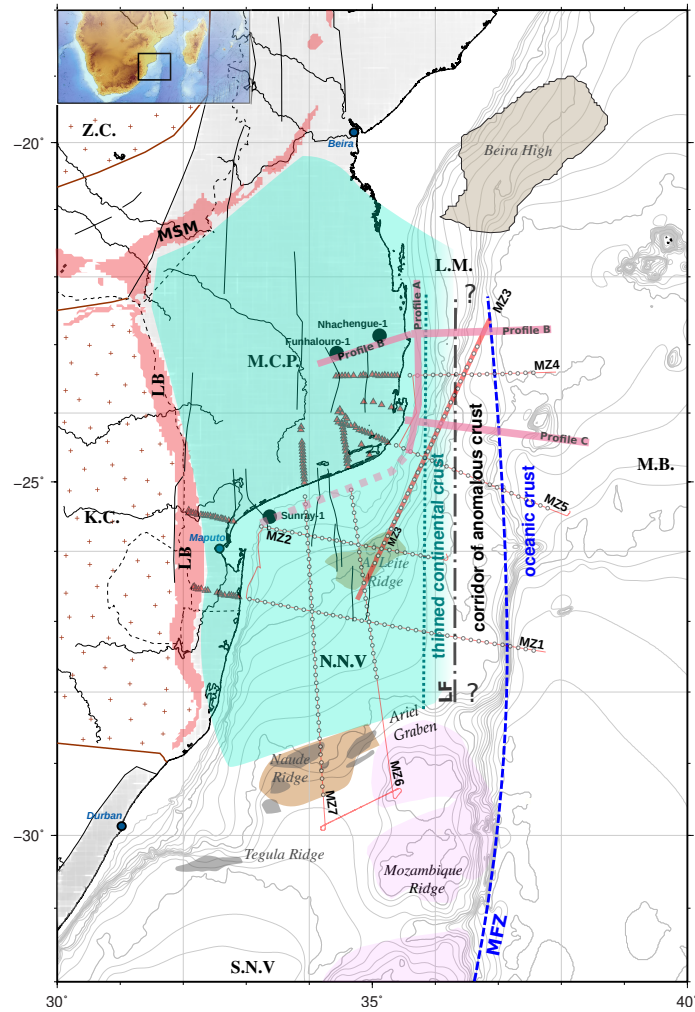


Figure 14. Map of the main segmentation and boundaries within our study area resulting from the combine interpretation of PAMELA-MOZ35 deep seismic profiles. Pink lines are locations of line drawings of commercial MCS profiles shown in figure 13. Background shows main onland geological units and structures: KC: Kaapval Craton; LB: Lebombo monocline; MSM: Mateke Sabi Monocline; MCP: Mozambique Coastal Plain; NNV: North Natal Valley; ZC: Zimbabwe Craton. Offshore bathymetric contours in the LM: Limpopo Margin; Mozambique Basin (MB) and South Natal Valley (SNV) and main geological features: Almirante Leite Ridge (ALR), Beira continental block or high (BH), Limpopo Fault (LF); Mozambique Ridge (MR), Mozambique Fracture Zone (MFZ), Tegula and Naude ridges, Ariel Graben (AG). MOZ35 seismic acquisition in the NNV and LM is shown in red with MZ3 profile highlighted in a bold red line.

the basement high at 330 km model distance. Beyond 340 km model distance, our velocity model only constrains a single layer
 385 (a prolongation of SV1 for modeling purpose) which is 1.5 km thick with intermediate velocities of 5.0-5.5 km/s. From these

velocities and its homogeneous, high amplitude but chaotic facies we suggest instead the presence of extruded volcanism only at the NE extremity of MZ3.

Commercial MCS data and companion PAMELA profiles complement and clarify the nature and extent of the deep volcano-sedimentary unit (SV1 and SV2). As for MZ3, all those profiles constrain a similar volcano-sedimentary unit (Moulin et al., 2020; Leprêtre et al., 2021; Schnürle et al., 2018) which ends oceanward in the form of a prominent basement high (Watremez et al.). Along PAMELA MOZ3-5 WAS profiles (MZ1, MZ6, MZ7) to the south-west, an identical unit in term of thickness and velocities consisting of parallel and undulating horizons is seen striking through the entire NNV before it dips oceanward to the south or east (Moulin et al., 2020; Leprêtre et al., 2021; Schnürle et al., 2018). At the southern LM, along MZ3 crossing profiles MZ5 (Watremez et al.) and C (brown color on Figure 13-Profile C) a broad basement high consists of internally gently dipping deformed but parallel reflectors. Further north, along MZ4 (Watremez et al.) and Profile B (Figure 13-Profile B) it is a set of landward dipping reflectors (LDR) that flanks the edge of the basement high. These LDR, however, connect with deep, wavy, and parallel horizons seen extending from the eastern MCP. There is therefore a connection and a prolongation of a volcano-sedimentary unit from the MCP, through the western LM and up to the NNV that is further highlighted along profile A where it is seen continuously all along the MCP coastline (Schnürle et al., 2018) (brown color on Figure 13-Profile A). All together these observations reveal that an ubiquitous volcano-sedimentary unit exists over our study area, from the south-eastern MCP to the entire NNV (in green on figures 14). We therefore suggest this unit forms a widespread pre-Neocomien basin that terminates to the east along the LM where it is strongly deformed and associated to prominent basement high and possibly deeply rooted faults.

5.3 Crustal nature and segmentation

Below the volcano-sedimentary basin, the top of the crystalline crust is higher at 4-5 km depth in the NNV than in the LM where it reaches 6-7 km depth on MZ3 (Figure 12). Considering the presence of a volcanic layer instead of a basin oceanward of the basement high, the top of the crystalline crust is there deeper at 7-7.5 km depth. Along the entire MZ3 profile this interface marks a velocity jump to values above 6 km/s that is responsible for a strong reflective phase observed on OBS records. Most importantly it is the place from which the velocity gradient of the crust becomes much lower around 0.044 km/s/km compared to the 0.25-0.3 km/s/km gradient within the upper acoustic basement.

Over the NNV (-50-110 km) the five layers that make the crystalline crust represent a 30 km thick unit with velocities between 6.0 km/s and 7.3 km/s top to bottom and a Moho lying at 34 km depth. Over the unthinned crust of the LM (up to 230 km) the same five layers represent a 24 km thick crust with a velocity range of 6.2-7.3 km/s and a 31 km deep Moho. The strong reflectivity of crustal phases observed on OBS records over both areas is responsible for the numerous layers modeled within the crust and mantle and attest of their important magmatic content. Crustal thinning occurs over a distance of 100 km to the SW of the basement high where the Moho rises from 31 km to 16 km deep (230-330 km). It coincides with a slight increase in velocity at the top of the crystalline basement (from 6.2 to 6.4 km/s) and a progressive decrease at its base (from 7.3 to 7.0 km/s). The velocity gradient remains thus stable and low (red cruves on figure 15b) while its internal highly reflective character is still observed. Therefore, despite crustal thinning, the overall structure of the NNV and western LM are similar

420 and consists of: an upper volcano-sedimentary basin, a low velocity gradient within the crystalline basement, strong magmatic intrusions, and anomalously high velocities at the base of the crust.

These characteristics are also those observed and highlighted on velocity models produced by companion studies along other PAMELA Moz3-5 profiles that either cross the MZ3 profile at the LM (Watremez et al.) or image the southeastern MCP and the NNV (Moulin et al., 2020; Schnürle et al., 2018; Leprêtre et al., 2021). Leprêtre et al. (2021) and Moulin et al. (2020) 425 have made an extensive comparison of the crustal structure of the MCP/NNV with published velocity structures of thickened oceanic crust or continental crust from different tectonic settings. They conclude on the continental nature of the MCP/NNV crust while the observed high velocities are explained by its strong magmatic content. By comparing 1-D velocity-depth (v_z) profiles extracted every 10 km along MZ3 with v_z profiles from MZ7 over both the MCP and NNV (Figure 15a-b) we can observe the coherence in crustal structure between the MCP, the NNV and the LM despite the latter progressive oceanward 430 thinning compared to normal continental crust (e.g. Christensen and Mooney, 1995). From the presence of a similar acoustic basement and similar crustal velocity profiles (v_z) we argue that the MCP/NNV continental crust further extends to the east under the LM at least up to location of the basement high (Figure 14). This interpretation contradicts previous studies that either consider this entire or parts of this region as floored by oceanic crust (e.g. Mueller and Jokat, 2019).

On the northeastern side of the basement high, the crystalline crust of the LM is only 10 km thick on MZ3 velocity model 435 (Figure 12). It is made of 3 layers with velocities between 6.5 km/s to 7.0 km/s top to bottom that show little internal reflectivity. While the two deepest layers present a low gradient (0.025 km/s/km) similar to the adjacent continental crystalline basement (Figure 15b), the upper layer has an intermediate velocity gradient (0.1 km/s/km) between those of the acoustic basement above and the deep crystalline basement below (Figure 15c). This anomalous trend is also observed on the ‘transitional crust’ identified on MZ4 and MZ5 (Watremez et al.) and east of the basement high on MZ1 velocity model (Moulin et al., 2020) as 440 shown by the comparison of v_z profiles from these profiles (Figure 15c). Taken all together they reveal a 60-80 km wide, N-S trending corridor of anomalous crust isolated between the thinned MCP and NNV continental crust to the west and the MB oceanic crust to the east (see corridor of anomalous crust on figure 14).

The basement high locates therefore an important segmentation in the crustal structure of the LM (Figure 14). Not only it coincides with the eastward termination of the volcano-sedimentary basin and a possible change in nature of the acoustic 445 basement but it also marks a profound modification of the crystalline crust. We can further notice that uppermost mantle velocities appears normal and stable at 8 km/s on each side of the basement high while a slight velocity decrease to 7.9 km/s (Figure 12), more pronounced on MZ4 and MZ5 velocity models (Watremez et al.) is present beneath the feature. This might suggest that the basement high is the surface expression of a vertical frontier that is deeply rooted in the lithosphere. As such it is comparable to the MFZ that bounds the opposite side of the corridor and separates it from the oceanic crust of the MB. We 450 therefore propose to refer to this zone of strongly localized deformation as the Limpopo Fault (LF, Figure 14).

To summarize, the LM is a N-S elongated margin cut by two major fault zones that segment its crustal structure in a western continental part, a central corridor and an eastern oceanic part (LF, Figure 14). The continental domain is the direct eastward prolongation of the continental crust that floor the MCP and NNV and capped by a pre-Neocomien volcano-sedimentary basin. Defining the nature of the crust within the corridor remains a challenge. V_z profiles (Figure 15c-d) reveal a possible mixed

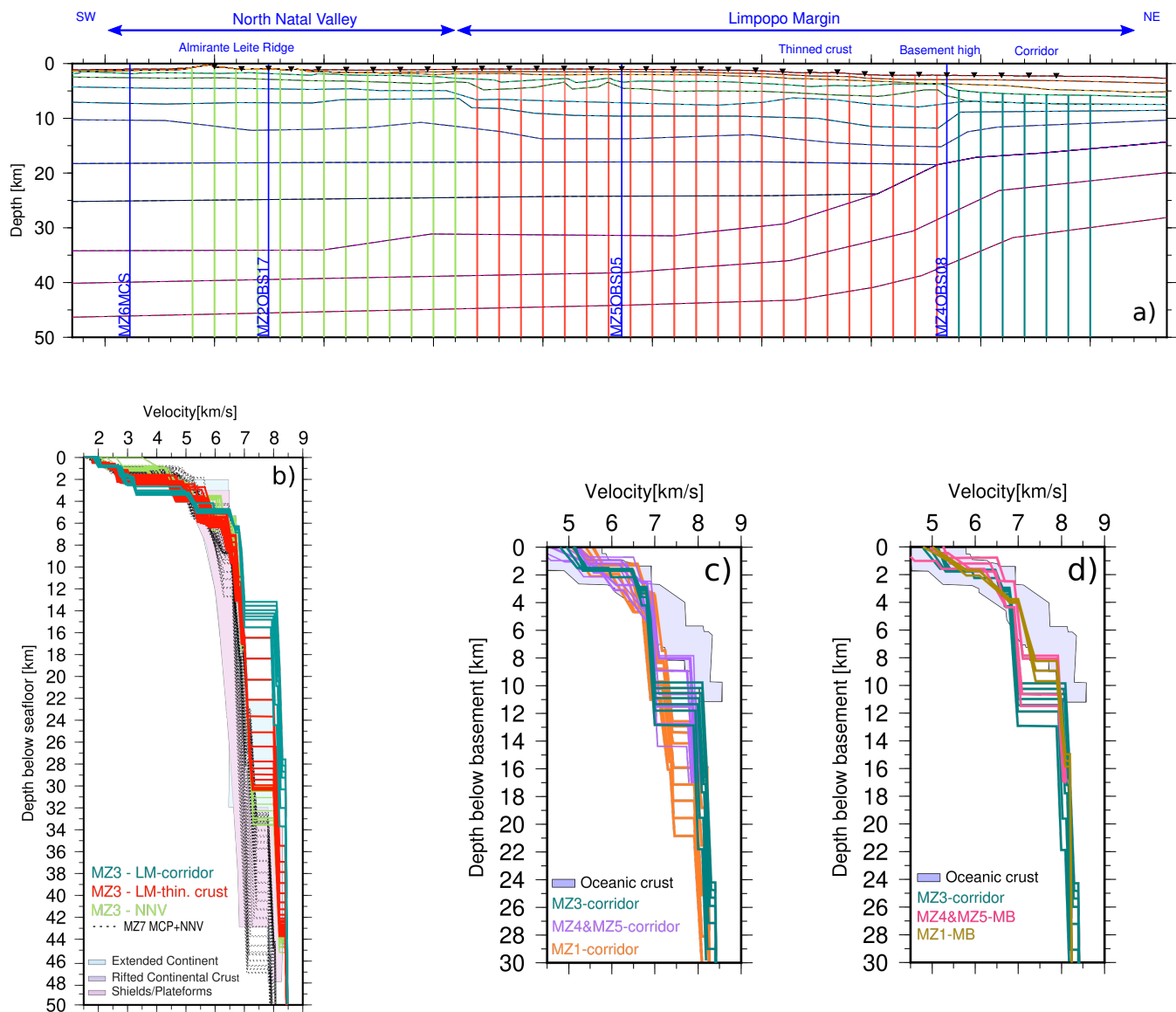


Figure 15. a) 1-D velocity-depth (v_z) profiles extracted along MZ3 final velocity model and color coded according to main domains and segments. b) MZ3 v_z profiles below seafloor compared to MZ7 v_z profiles of the MCP and NNV, and compiled v_z profiles of continental crust for different settings (Christensen and Mooney, 1995). c) Comparison of v_z profiles below the acoustic basement of the corridor of anomalous crust extracted from MZ1 (Moulin et al., 2020; Schnürle et al., 2018), MZ3 (this study), MZ4 and MZ5 (Watremez et al.) models with a compilation of v_z from ‘normal’ Atlantic oceanic crust (White et al., 1992). d) Comparison of MZ3 v_z profiles below the acoustic basement of the corridor of anomalous crust with v_z for the oceanic crust of the MB extracted from MZ1 (Moulin et al., 2020; Schnürle et al., 2018), MZ4 and MZ5 (Watremez et al.) and compared to the compilation of (White et al., 1992).

455 composition. On one hand a 3-4 km thick upper part with a typical signature of oceanic crust caused by the presence of extruded
volcanics. On the other hand a lower part that still preserve the low gradient characteristics of adjacent continental crust. Its
crustal thickness is also extremely variable (5 to 15 km) and appears thicker to the south (MZ1) than to the north (MZ3, MZ4,
MZ5: Figure 15c). Vz of the MB oceanic crust located just east of the MFZ also show some changes with a velocity signature
close to the corridor to the north where it is the oldest and a signature that shift toward typical oceanic crust to the south (Figure
460 15d).

6 Discussion

6.1 Geodynamic implications

Deep crustal velocity models produced from the PAMELA-MOZ35 seismic experiment have revealed the presence of a 40 km
and 30 km thick crust respectively beneath the southern MCP and offshore NNV (Moulin et al., 2020; Schnürle et al., 2018;
465 Leprêtre et al., 2021). They also show a continuous and mildly deformed volcano-sedimentary cover over these two entities.
These findings are strong evidence in favor of a continental nature of the MCP/NNV as suggested previously by seismological
and magnetic studies (Domingues et al., 2016; Hanyu et al., 2017). This work further precises the crustal architecture of the
area, delimiting the eastern edge of this continental unit along the LM. The presence of an homogeneous basin over a thick
continental crust attest of an intra-continental depositional process (Moulin et al., 2020) rather than a rifted margin process (e.g.
470 Cox, 1992; Klausen, 2009; Watkeys, 2002). Our tectono-stratigraphic analysis only place an upper bound to the formation of the
basin in pre-Neocomian. So far it has not been dated more precisely despite that its upper volcanic layer was reached by several
wells (Flores, 1973). We can thus speculate that it formed during the Karoo phase which affected the entire African continent
in late Palaeozoic/early Triassic (Daly et al., 1991). However, this would leave a large, 30 My, sedimentary gaps between
extrusions of Karoo volcanics, which might compose the roof of the basin, and deposition of late-Jurassic to Neocomien
475 Red Beds and Cretaceous Maputo formations. Therefore, another hypothesis is that it formed in late-Jurassic either before or
contemporaneously with the formation of the adjacent MB as suggested by (Li et al., 2021). The high magmatic content of the
basin as well as evidence of strongly intruded continental crust suggest that magmatism may have overloaded the crust and
created the necessary vertical subsidence (Moulin et al., 2020; Tozer et al., 2017).

Our study also emphasizes the eastward prolongation and termination of the volcano-sedimentary basin along the LM where
480 it is strongly deformed by deeply rooted vertical faults. At depth, it is also the place where important crustal thinning and
segmentation is evidenced (Figure 14). Therefore the LM appears naturally as the place where rifting localized to accommodate
the opening of the MB rather than over then entire MCP/NNV. In previous scenarios based on 'tight' fit kinematic framework in
which Antarctica partly overlaps Africa, rifting was either postulated to concentrate along the Lebombo monocline or beneath
the MCP/NNV depending whether the area was interpreted as oceanic or a volcanic rifted margin (Cox, 1992; Klausen, 2009;
485 Leinweber and Jokat, 2012; Mueller and Jokat, 2019; Watkeys, 2002). Neither of these hypothesis are supported by these new
observations.

Overall, this means that the MCP/NNV must be excluded from the Africa-Antarctica corridor (AAC in Leinweber and Jokat, 2012; Mueller and Jokat, 2019) and a ‘looser’ plate fit must be adopted in East-Gondwana kinematic reconstruction (Moulin et al., 2020; Thompson et al., 2019). Such framework excludes any initial rifting phase with normal (E-W) or oblique (NW-SE) plates movement (e.g. Cox, 1992; Reeves et al., 2016) which, to our opinion, has never been clearly evidenced or described. Invoking indeed the orientation of magmatic dyke swarms to attest stress field direction (Mueller and Jokat, 2019; Reeves et al., 2016) is highly speculative as they may be strongly controlled by inherited lithospheric discontinuities (Jourdan et al., 2006). Similarly, the presence of a wide crustal necking zone cannot solely justify normal or oblique rifting (e.g. Vormann et al., 2020). Indeed the LM itself shows such characteristics but given our preferred and alternative geodynamic framework it was affected instead by strike-slip or slightly trans-tensional rifting following a continuous N-S direction of plate motions during the opening of the MB.

6.2 Strike-slip rifting along the Limpopo Margin

Along the LM, strike-slip rifting is emphasized by the Limpopo Fault (Figure 14). It forms a zone of deeply rooted and strongly localized deformation rising to the surface as a flower structure (Figure 3,13). Basement uplift is evidenced by the presence of a prominent high along the fault with deposition of pre-Neocomian Red Beds on either side and signs of erosion of the Maputo Sands formation that covers it. Taking all together these indicators reflect strike-slip strain along the LF which lasted up to early Cretaceous. Despite a thick sedimentary cover and strong magmatic content which affect the definition of seismic profiles we identified a long wavelength wavy deformation within the volcano-sedimentary basement that looks like folding as well as a few horsts and grabens (Figure 3,13). Those are located at the western edge of the LM and might reflect some partitioning in the deformation of the upper crust with a slight normal component. Uplifts, en-echelon pull-apart structures and shear foldings are typical features so far observed along highly oblique or strike-slip margins (e.g. Mascle and Blarez, 1987) but more generally those contexts are favorable to strain partitioning and a wide range of deformation features (Brune, 2014; Teyssier et al., 1995).

Besides upper crustal brittle deformations of the LM during its rifting our observations point toward important crustal reworking at depth accompanied by volcanic extrusions. From the thinned continental crust structure to the west of LM and the lower continental crust velocity signature of the anomalous corridor (Figure 12, but see also MZ1 model in (Moulin et al., 2020; Schnürle et al., 2018) we infer that oceanward flow of the MCP and NNV lower crust may have ‘fed’ the corridor. The corridor’s crystalline basement is 10-12 km thick on MZ3 (Figure 15c) in the northernmost LM, varies from 8 to 14 km thick offshore the MCP (MZ4 and MZ5 on figure 15c) and thickens to 15-20 km thick east of the NNV (MZ1 on figure 15c). Such variation in thickness may be evidence of the ‘boudinage’ of the lower crust originating from its ductile shearing and flow (Clerc et al., 2018; Gernigon et al., 2014; Loureiro et al., 2018). Strong volcanism has accompanied this process as suggested by the ‘mixed’ composition of the corridor and time constraints given by the deposition on top of these volcanics of the Maputo Sands which preceded the first deep marine sedimentation (Figure 13).

Lower continental crust flow/shearing, eventually leading to exhumation (Aslanian et al., 2009), has been inferred in many places including offshore eastern Canada and Arctic margins (Gernigon et al., 2014; Reid and Jackson, 1997), along South-

Atlantic Brazilian (Evain et al., 2015; Loureiro et al., 2018) and western African margins (Clerc et al., 2018; Moulin et al., 2005), offshore Mozambique (Senkans et al., 2019); and in the Mediterranean Sea Gulf of Lion and Sardinian margins (Afilhado et al., 2015; Moulin et al., 2015; Jolivet et al., 2015). It appears as a common process of rifted continental margin independently of their tectonic context. In fact it has been shown numerically that lower crust may flow across both divergent margin segments (Huismans and Beaumont, 2011) and strike-slip segments (Le Pourhiet et al., 2017; Reid, 1989). Usually it is noticed that weak lower crust may favor such exhumation process. It was undoubtedly the case for the southern-Mozambique lithosphere which on the verge of its dislocation was affected by a large thermal anomaly (Karoo?) responsible for its anomalous magmatic content. The same anomaly might have favored coeval partial melting and extrusion of volcanic material to form the volcanic basement of the corridor.

6.3 Rift to drift evolution and vertical movements

In the alternative East-Gondwana ‘fit’ proposed by Thompson et al. (2019), the continental domain to the south-west of the Astrid Ridge on the Antarctica plate is the conjugate of the African corner made by the MCP and the Beira High (Figure 16a-b). Further south the Grunneghona craton is facing the NNV. The exact seaward limit of the Antarctica continental crust is inferred at the location of a strong positive free-air gravity anomaly (Mueller and Jokat, 2019; Scheinert et al., 2016) since transitional crust is observed further offshore on seismic data (Jokat et al., 2004). At this stage, the Antarctica plate overlaps the corridor which will develop progressively during rifting (Figure 16b) and before oceanic spreading in the MB starts from Chron M25 (155 Ma) onwards (Figure 16c-d). As discussed above we infer an intra-continental sag phase for the development of the volcano-sedimentary basin over the MCP and NNV. Deep crustal magmatic intrusions led to the subsidence of the area without major plate movements (Moulin et al., 2020). On the other hand, rifting along the LM proceeded from an almost N-S plate motion responsible for the opening of the MB (Figure 16b-c). The LM developed as a wide shear zone along the eastern margin of the MCP and NNV. The LF acted at this time as a major strike-slip fault while easing the decoupling between upper and lower crust at depth. In the upper crust we infer that strain partitioning is responsible for shear folds, small pull-apart basins and grabens within the volcano-sedimentary basement. Deeper, extension was accommodated by lithospheric flow leading to lower crustal thinning of the eastern fringe of MCP/NNV continental crust and its oceanward exhumation. This was accompanied by the extrusion of a large amount of volcanics over the corridor. Further west, deep seismic acquisition revealed a transitional domain capped by a thick volcanic layer (the Explora Wedge, e.g. Jokat et al., 2004) off the Antarctic margin which might attest of an equivalent process, thought along a divergent segment. On the African side, extension initially focused in the offshore Zambezi depression before migrating to the south of the Beira High, isolating this continental block (Mahanjane, 2012). The nature of the crust to the north of the Beira High is also deemed to be transitional with syn-rift magmatism reported (Mueller et al., 2016; Mueller and Jokat, 2019).

According to our stratigraphic analysis, scarce Red Beds continental sedimentation was followed by the widespread deposition of shallow marine Maputo Sands over both the MCP/NNV and LM. Only then, the eastern extremity of the corridor was covered by the first deep marine sediments. Lithospheric and/or asthenospheric flow may have sustained the area to a relative high level during continental rifting (Reid, 1989) allowing continental Red Beds deposits first, then slight subsidence respon-

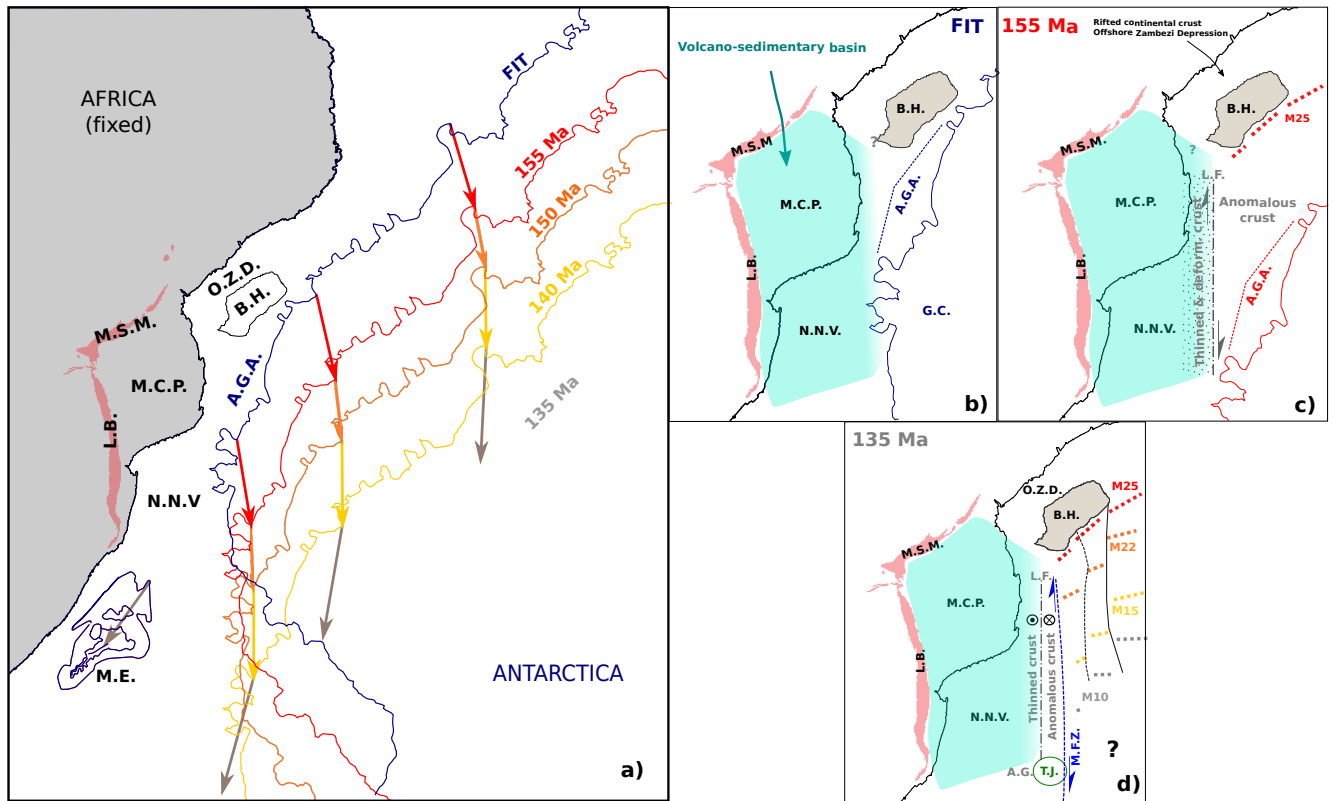


Figure 16. Evolution of the Limpopo Margin (LM). a) Kinematic of the Antarctica plate with respect to the African plate fixed according to (Thompson et al., 2019). b,c,d) Zooms on the evolution of the LM with major features annotated respectively before rifting (b), at break-up (c) and after the opening of the Mozambique Basin along the LM (d). Magnetic anomalies are from Mueller and Jokat (2019). LB: Lebombo monocline; MSM: Mateke Sabi Monocline; MCP: Mozambique Coastal Plain; NNV: North Natal Valley; ME: Maurice Ewing bank; BH: Beira high, OZD: Offshore Zambezi Depression AGA: Antractic Gravity Anomaly; GC: Grunehogna Craton; LF: Limpopo Fault; MFZ: Mozambique Fracture Zone, AG: Ariel Graben. TJ: Triple Junction.

555 sible for the first shallow marine incursion. Minor vertical movements must have occurred along the LF only due to strike-slip shearing. It is some times after break-up that larger differential vertical movement took place on either side of the LF between the continental domain and the corridor, hence accentuating the basement high and limiting the westward incursion of the first deep marine sedimentary horizons.

As in previous studies (see Basile, 2015, and references therein) we recognize that a stage of continent-ocean interaction
560 followed continental rifting and its break-up. Analyzing the possible interplay between the corridor and the mid-oceanic ridge

requires, however, a careful analysis of later stratigraphic horizons across and all along the margin which is out of the scope of our study. Figure 16c to 16d illustrates the drift of the mid-ocean ridge axis through time based on identified magnetic chrons (Mueller and Jokat, 2019, and references therein). Valanginian (Figure 16d) corresponds to a period of major kinematic reorganization in the area. While the Patagonian block started its southwestward drift, a triple junction initiated responsible for enhanced magmatism and the formation of the Mozambique ridge (Fischer et al., 2017). At this time the mid-oceanic ridge axis reached the position of the Ariel Graben. Active deformation thus ceased along the LM which entered in a passive stage and progressively acquired its present morphology.

7 Conclusions

This study focuses on the MZ3 combined MCS and WAS profile acquired across the LM within the scope of the PAMELA MOZ3-5 project. A p-wave velocity model of the deep crustal architecture of the margin is produced and interpreted with additional inputs from a tectono-stratigraphic analysis of industrial seismic profiles and adjacent velocity models from companion studies (Moulin et al., 2020; Schnürle et al., 2018; Lepretre et al., 2021; Watremez et al.). We evidence the eastern prolongation, thinning and termination of the MCP/NNV continental crust under the LM. We further highlight its segmentation emphasized by the presence of a N-S oriented corridor of anomalous crust bounded by deeply rooted faults, i.e the Limpopo fault to the west and the MFZ to the east. Consistently with recent plate kinematic reconstruction of East-Gondwana break-up we infer that strike-slip or highly oblique rifting occurred along the LM. This led to the thinning of the continental crust beneath the eastern edge of the MCP/NNV while the observed peculiar ‘mixed’ crustal composition of the corridor is explained by lower crust flow with additional magmatic inputs. Finally, we show that only moderate subsidence occurred during the intra-continental rifting and early continent-ocean interaction stages. It is only after the break-up that decoupling along the LF led to differential vertical motion on each side of the fault with uplift of the continental domain while subsidence affected the corridor.

Data availability. Seismic datasets of the PAMELA-MOZ3 (Moulin and Aslanian, 2016) and PAMELA-MOZ5 (Moulin and Evain, 2016) cruises are archived and referenced in Ifremer SISMER database and can be requested at:

<https://doi.org/10.17600/16009500> and <https://doi.org/10.17600/16001600>.

MZ3 final velocity model is provided in RAYINVR format on SEANOE at <https://doi.org/10.17882/80287> (Evain Mikael, 2021)

Author contributions. The Pamela MOZ35 project was led by M. Moulin, D. Aslanian and M. Evain from Ifremer in collaboration with Total. Modelling of profiles MZ1 and MZ7 was done by A. Lepretre ; MZ2 by F. Verrier and P. Schnürle, MZ3 by M. Evain, profiles MZ4 and MZ5 by L. Watremez and MZ6 by P. Schnürle. Processing of the deep-sounding reflection seismic data was done by P. Schnürle. M. Evain wrote the article with valuable inputs from all co-authors.

Competing interests. The authors declare that they have no known competing financial interests or personal relationships that could have
590 appeared to influence the work reported in this paper.

Acknowledgements. We thank the captain, crew, and MCS technical team of the R/V Pourquoi-Pas. We also thank the OBS technical team who maintain and constantly improve our OBS pool, as well as the land stations deployment team. A Leprêtre and F. Verrier respective post-doc studies and contract were co-funded by TOTAL and Ifremer as part of the PAMELA (Passive Margin Exploration Laboratories) scientific project. We thanks WesternGeco, INP and Total for permission to make and publish line-drawings of seismic data. The GMT
595 (Wessel and Smith, 1998), Seismic Unix (Cohen and Stockwell, 2019; Stockwell, 1999), and Geocluster (CGG-Veritas) software packages were used extensively in this study.

References

- Adam, J. M.-C. and Lebedev, S.: Azimuthal anisotropy beneath southern Africa from very broad-band surface-wave dispersion measurements, *Geophysical Journal International*, 191, 155–174, <https://doi.org/10.1111/j.1365-246X.2012.05583.x>, <https://onlinelibrary.wiley.com/doi/abs/10.1111/j.1365-246X.2012.05583.x>, 2012.
- Afilhado, A., Moulin, M., Aslanian, D., Schnürle, P., Klingelhoefer, F., Nouzé, H., Rabineau, M., Leroux, E., and Beslier, M.-O.: Deep crustal structure across a young passive margin from wide-angle and reflection seismic data (The SARDINIA Experiment) – II. Sardinia’s margin, *Bulletin de la Société Géologique de France*, 186, 331–351, <https://doi.org/10.2113/gssgfbull.186.4-5.331>, <https://pubs.geoscienceworld.org/sgf/bsgf/article/186/4-5/331/285718/Deep-crustal-structure-across-a-young-passive>, 2015.
- Aslanian, D., Moulin, M., Olivet, J.-L., Unternehr, P., Matias, L., Bache, F., Rabineau, M., Nouzé, H., Klingelhoefer, F., Contrucci, I., and Labails, C.: Brazilian and African passive margins of the Central Segment of the South Atlantic Ocean: Kinematic constraints, *Tectonophysics*, 468, 98–112, <https://doi.org/10.1016/j.tecto.2008.12.016>, <https://linkinghub.elsevier.com/retrieve/pii/S0040195108006252>, 2009.
- Baby, G.: Mouvements verticaux des marges passives d’Afrique australe depuis 130 Ma, étude couplée : stratigraphie de bassin : analyse des formes du relief, Ph.D. thesis, Université Rennes 1, 2017.
- Baby, G., Guillocheau, F., Boulogne, C., Robin, C., and Dall’Asta, M.: Uplift history of a transform continental margin revealed by the stratigraphic record: The case of the Agulhas transform margin along the Southern African Plateau, *Tectonophysics*, 731-732, 104–130, <https://doi.org/10.1016/j.tecto.2018.03.014>, <http://linkinghub.elsevier.com/retrieve/pii/S0040195118301197>, 2018.
- Basile, C.: Transform continental margins — part 1: Concepts and models, *Tectonophysics*, 661, 1–10, <https://doi.org/10.1016/j.tecto.2015.08.034>, <http://linkinghub.elsevier.com/retrieve/pii/S0040195115004618>, 2015.
- Ben-Avraham, Z., Hartnady, C. J. H., and Roex, A. P. I.: Neotectonic activity on continental fragments in the South-west Indian Ocean: Agulhas Plateau and Mozambique Ridge, *Journal of Geophysical Research: Solid Earth*, 100, 6199–6211, <https://doi.org/10.1029/94JB02881>, <https://agupubs.onlinelibrary.wiley.com/doi/abs/10.1029/94JB02881>, [_eprint: https://agupubs.onlinelibrary.wiley.com/doi/pdf/10.1029/94JB02881](https://agupubs.onlinelibrary.wiley.com/doi/pdf/10.1029/94JB02881), 1995.
- Bingen, B., Jacobs, J., Viola, G., Henderson, I. H. C., Skår, , Boyd, R., Thomas, R. J., Solli, A., Key, R. M., and Daudi, E. X. F.: Geochronology of the Precambrian crust in the Mozambique belt in NE Mozambique, and implications for Gondwana assembly, *Precambrian Research*, 170, 231–255, <https://doi.org/10.1016/j.precamres.2009.01.005>, <http://www.sciencedirect.com/science/article/pii/S0301926809000229>, 2009.
- Brune, S.: Evolution of stress and fault patterns in oblique rift systems: 3-D numerical lithospheric-scale experiments from rift to breakup, *Geochemistry, Geophysics, Geosystems*, 15, 3392–3415, <https://doi.org/10.1002/2014GC005446>, <https://agupubs.pericles-prod.literatumonline.com/doi/abs/10.1002/2014GC005446>, [_eprint: https://agupubs.onlinelibrary.wiley.com/doi/pdf/10.1002/2014GC005446](https://agupubs.onlinelibrary.wiley.com/doi/pdf/10.1002/2014GC005446), 2014.
- Catuneanu, O.: Basement control on flexural profiles and the distribution of foreland facies: The Dwyka Group of the Karoo Basin, South Africa, *Geology*, 32, 517–520, <https://doi.org/10.1130/G20526.1>, <https://pubs.geoscienceworld.org/geology/article-abstract/32/6/517/29470/Basement-control-on-flexural-profiles-and-the>, publisher: GeoScienceWorld, 2004.
- Christensen, N. I. and Mooney, W. D.: Seismic velocity structure and composition of the continental crust: A global view, *Journal of Geophysical Research: Solid Earth*, 100, 9761–9788, <https://doi.org/10.1029/95JB00259>, <http://doi.wiley.com/10.1029/95JB00259>, 1995.

- Clerc, C., Ringenbach, J.-C., Jolivet, L., and Ballard, J.-F.: Rifted margins: Ductile deformation, boudinage, continentward-dipping normal faults and the role of the weak lower crust, *Gondwana Research*, 53, 20–40, <https://doi.org/10.1016/j.gr.2017.04.030>, <http://www.sciencedirect.com/science/article/pii/S1342937X17302150>, 2018.
- Cohen, J. and Stockwell, J. J. W.: CWP/SU: Seismic Un*xRelease No.44: an open source software package for seismicresearch and processing, 2019.
- Courgeon, S., Bachèlery, P., Jouet, G., Jorry, S. J., Bou, E., BouDagher-Fadel, M. K., Révillon, S., Camoin, G., and Poli, E.: The offshore east African rift system: new insights from the Sakalaves seamounts (Davie Ridge, SW Indian Ocean), *Terra Nova*, 0, <https://doi.org/10.1111/ter.12353>, <https://onlinelibrary.wiley.com/doi/abs/10.1111/ter.12353>, 2018.
- Cox, K. G.: Karoo igneous activity, and the early stages of the break-up of Gondwanaland, Geological Society, London, Special Publications, 68, 137–148, <https://doi.org/10.1144/GSL.SP.1992.068.01.09>, <http://sp.lyellcollection.org/content/68/1/137>, 1992.
- Daly, M. C., Chorowicz, J., and Fairhead, J. D.: Rift basin evolution in Africa: the influence of reactivated steep basement shear zones, Geological Society, London, Special Publications, 44, 309–334, <https://doi.org/10.1144/GSL.SP.1989.044.01.17>, <https://sp.lyellcollection.org/content/44/1/309>, 1989.
- Daly, M. C., Lawrence, S. R., Kimun’a, D., and Binga, M.: Late Palaeozoic deformation in central Africa: a result of distant collision?, *Nature*, 350, 605–607, <https://doi.org/10.1038/350605a0>, <https://www.nature.com/articles/350605a0>, 1991.
- Deville, E., Marsset, T., Courgeon, S., Jatiault, R., Ponte, J.-P., Thereau, E., Jouet, G., Jorry, S. J., and Droz, L.: Active fault system across the oceanic lithosphere of the Mozambique Channel: Implications for the Nubia–Somalia southern plate boundary, *Earth and Planetary Science Letters*, 502, 210–220, <https://doi.org/10.1016/j.epsl.2018.08.052>, <http://www.sciencedirect.com/science/article/pii/S0012821X18305181>, 2018.
- Dingle, R. V. and Scrutton, R. A.: Continental Breakup and the Development of Post-Paleozoic Sedimentary Basins around Southern Africa, *GSA Bulletin*, 85, 1467–1474, [https://doi.org/10.1130/0016-7606\(1974\)85<1467:CBATDO>2.0.CO;2](https://doi.org/10.1130/0016-7606(1974)85<1467:CBATDO>2.0.CO;2), [https://doi.org/10.1130/0016-7606\(1974\)85<1467:CBATDO>2.0.CO;2](https://doi.org/10.1130/0016-7606(1974)85<1467:CBATDO>2.0.CO;2), 1974.
- Domingues, A., Silveira, G., Ferreira, A. M., Chang, S.-J., Custódio, S., and Fonseca, J. F.: Ambient noise tomography of the East African Rift in Mozambique, *Geophysical Journal International*, 204, 1565–1578, <https://doi.org/10.1093/gji/ggv538>, <https://academic.oup.com/gji/article-lookup/doi/10.1093/gji/ggv538>, 2016.
- Elliot, D. H. and Fleming, T. H.: Occurrence and Dispersal of Magmas in the Jurassic Ferrar Large Igneous Province, Antarctica, *Gondwana Research*, 7, 223–237, [https://doi.org/10.1016/S1342-937X\(05\)70322-1](https://doi.org/10.1016/S1342-937X(05)70322-1), <http://www.sciencedirect.com/science/article/pii/S1342937X05703221>, 2004.
- Evain, M., Afilhado, A., Rigoti, C., Loureiro, A., Alves, D., Klingelhoefer, F., Schnurle, P., Feld, A., Fuck, R., Soares, J., de Lima, M. V., Corela, C., Matias, L., Benabdellouahed, M., Baltzer, A., Rabineau, M., Viana, A., Moulin, M., and Aslanian, D.: Deep structure of the Santos Basin–São Paulo Plateau System, SE Brazil: Santos Basin–São Paulo Plateau Structure, *Journal of Geophysical Research: Solid Earth*, 120, 5401–5431, <https://doi.org/10.1002/2014JB011561>, <http://doi.wiley.com/10.1002/2014JB011561>, 2015.
- Evain Mikael, Schnurle Philippe, L. A. V. F. W. L. T. J. O. D.-C. P. A. D. M. M.: Crustal structure of the East-African Limpopo Margin, a strike-slip rifted corridor along the continental Mozambique Coastal Plain and North-Natal Valley, SEANOE, <https://doi.org/10.17882/80287>, <https://www.seanoe.org/data/00691/80287/>, 2021.
- Fischer, M. D., Uenzelmann-Neben, G., Jacques, G., and Werner, R.: The Mozambique Ridge: a document of massive multistage magmatism, *Geophysical Journal International*, 208, 449–467, <https://doi.org/10.1093/gji/ggw403>, <https://academic.oup.com/gji/article/208/1/449/2417316>, 2017.

- Flores, G.: The Cretaceous and Tertiary basins of Mozambique and Zululand, in: *Sedimentary Basins of the African Coast*, Paris, ass. afr. geol. surveys edn., 1973.
- Geiger, M., Clark, D. N., and Mette, W.: Reappraisal of the timing of the breakup of Gondwana based on sedimentological and seismic evidence from the Morondava Basin, Madagascar, *Journal of African Earth Sciences*, 38, 363–381, <https://doi.org/10.1016/j.jafrearsci.2004.02.003>, <http://www.sciencedirect.com/science/article/pii/S0899536204000302>, 2004.
- Gernigon, L., Brönnner, M., Roberts, D., Olesen, O., Nasuti, A., and Yamasaki, T.: Crustal and basin evolution of the southwestern Barents Sea: From Caledonian orogeny to continental breakup, *Tectonics*, 33, 347–373, <https://doi.org/10.1002/2013TC003439>, <https://agupubs.onlinelibrary.wiley.com/doi/abs/10.1002/2013TC003439>, <https://agupubs.onlinelibrary.wiley.com/doi/pdf/10.1002/2013TC003439>, 2014.
- Gohl, K., Uenzelmann-Neben, G., and Grobys, N.: GROWTH AND DISPERSAL OF A SOUTHEAST AFRICAN LARGE IGNEOUS PROVINCE, *South African Journal of Geology*, 114, 379–386, <https://doi.org/10.2113/gssajg.114.3-4.379>, <https://pubs.geoscienceworld.org/sajg/article-abstract/114/3-4/379/141401/GROWTH-AND-DISPERSAL-OF-A-SOUTHEAST-AFRICAN-LARGE>, 2011.
- Goodlad, S. W.: Tectonic and sedimentary history of the Mid-Natal Valley (S.W. Indian Ocean), <http://hdl.handle.net/11427/23640>, publisher: University of Cape Town, 1986.
- Goodlad, S. W., Martin, A. K., and Hartnady, C. J. H.: Mesozoic magnetic anomalies in the southern Natal Valley, *Nature*, 295, 686–688, <https://doi.org/10.1038/295686a0>, <https://www.nature.com/articles/295686a0>, 1982.
- Green, A. G.: Seafloor Spreading in the Mozambique Channel, *Nature Physical Science*, 236, 19–21, <https://doi.org/10.1038/physci236019a0>, <https://www.nature.com/articles/physci236019a0>, number: 63 Publisher: Nature Publishing Group, 1972.
- Guiraud, R., Bosworth, W., Thierry, J., and Delplanque, A.: Phanerozoic geological evolution of Northern and Central Africa: An overview, *Journal of African Earth Sciences*, 43, 83–143, <https://doi.org/10.1016/j.jafrearsci.2005.07.017>, <http://www.sciencedirect.com/science/article/pii/S1464343X05001147>, 2005.
- Hanyu, T., Nogi, Y., and Fujii, M.: Crustal formation and evolution processes in the Natal Valley and Mozambique Ridge, off South Africa, *Polar Science*, 13, 66–81, <https://doi.org/10.1016/j.polar.2017.06.002>, <http://www.sciencedirect.com/science/article/pii/S1873965217300117>, 2017.
- Hartnady, C., Ben-Avraham, Z., and Rogers, J.: Deep-ocean basins and submarine rises off the continental margin of south-eastern Africa: new geological research, 88, 534–539, 1992.
- Hastie, W. W., Watkeys, M. K., and Aubourg, C.: Magma flow in dyke swarms of the Karoo LIP: Implications for the mantle plume hypothesis, *Gondwana Research*, 25, 736–755, <https://doi.org/10.1016/j.gr.2013.08.010>, <http://www.sciencedirect.com/science/article/pii/S1342937X13002839>, 2014.
- Huisman, R. and Beaumont, C.: Depth-dependent extension, two-stage breakup and cratonic underplating at rifted margins, *Nature*, 473, 74–78, <https://doi.org/10.1038/nature09988>, <http://www.nature.com/articles/nature09988>, 2011.
- Jacobs, J. and Thomas, R. J.: Himalayan-type indenter-escape tectonics model for the southern part of the late Neoproterozoic–early Paleozoic East African–Antarctic orogen, *Geology*, 32, 721–724, <https://doi.org/10.1130/G20516.1>, <https://pubs.geoscienceworld.org/gsa/geology/article/32/8/721/29547/Himalayan-type-indenter-escape-tectonics-model-for>, publisher: GeoScienceWorld, 2004.
- Jacobs, J., Pisarevsky, S., Thomas, R. J., and Becker, T.: The Kalahari Craton during the assembly and dispersal of Rodinia, *Precambrian Research*, 160, 142–158, <https://doi.org/10.1016/j.precamres.2007.04.022>, <http://www.sciencedirect.com/science/article/pii/S0301926807001611>, 2008.

- Jokat, W., Boebel, T., König, M., and Meyer, U.: Timing and geometry of early Gondwana breakup, *Journal of Geophysical Research: Solid Earth*, 108, <https://doi.org/10.1029/2002JB001802>, <https://agupubs.onlinelibrary.wiley.com/doi/abs/10.1029/2002JB001802>, 2003.
- Jokat, W., Ritzmann, O., Reichert, C., and Hinz, K.: Deep Crustal Structure of the Continental Margin off the Explora Escarpment and in the Lazarev Sea, East Antarctica, *Marine Geophysical Researches*, 25, 283–304, <https://doi.org/10.1007/s11001-005-1337-9>, <http://link.springer.com/10.1007/s11001-005-1337-9>, 2004.
- Jolivet, L., Gorini, C., Smit, J., and Leroy, S.: Continental breakup and the dynamics of rifting in back-arc basins: The Gulf of Lion margin: Backarc rift and lower crust extraction, *Tectonics*, 34, 662–679, <https://doi.org/10.1002/2014TC003570>, <http://doi.wiley.com/10.1002/2014TC003570>, 2015.
- Jourdan, F., Féraud, G., Bertrand, H., Kampunzu, A. B., Tshoso, G., Watkeys, M. K., and Gall, B. L.: Karoo large igneous province: Brevity, origin, and relation to mass extinction questioned by new 40Ar/39Ar age data, *Geology*, 33, 745–748, <https://doi.org/10.1130/G21632.1>, <https://pubs.geoscienceworld.org/geology/article/33/9/745/29633/Karoo-large-igneous-province-Brevity-origin-and>, 2005.
- Jourdan, F., Féraud, G., Bertrand, H., Watkeys, M. K., Kampunzu, A. B., and Le Gall, B.: Basement control on dyke distribution in Large Igneous Provinces: Case study of the Karoo triple junction, *Earth and Planetary Science Letters*, 241, 307–322, <https://doi.org/10.1016/j.epsl.2005.10.003>, <http://www.sciencedirect.com/science/article/pii/S0012821X05006801>, 2006.
- Jourdan, F., Féraud, G., Bertrand, H., Watkeys, M. K., and Renne, P. R.: Distinct brief major events in the Karoo large igneous province clarified by new 40Ar/39Ar ages on the Lesotho basalts, *Lithos*, 98, 195–209, <https://doi.org/10.1016/j.lithos.2007.03.002>, <http://www.sciencedirect.com/science/article/pii/S0024493707000515>, 2007.
- Klausen, M. B.: The Lebombo monocline and associated feeder dyke swarm: Diagnostic of a successful and highly volcanic rifted margin?, *Tectonophysics*, 468, 42–62, <https://doi.org/10.1016/j.tecto.2008.10.012>, <http://www.sciencedirect.com/science/article/pii/S0040195108005040>, 2009.
- König, M. and Jokat, W.: Advanced insights into magmatism and volcanism of the Mozambique Ridge and Mozambique Basin in the view of new potential field data, *Geophysical Journal International*, 180, 158–180, <https://doi.org/10.1111/j.1365-246X.2009.04433.x>, <https://academic.oup.com/gji/article-lookup/doi/10.1111/j.1365-246X.2009.04433.x>, 2010.
- Lafourcade, P.: Etude géologique et géophysique de la marge continentale du sud Mozambique (17 S à 28 S), PhD Thesis, 1984.
- Le Pourhiet, L., May, D. A., Huille, L., Watremez, L., and Leroy, S.: A genetic link between transform and hyper-extended margins, *Earth and Planetary Science Letters*, 465, 184–192, <https://doi.org/10.1016/j.epsl.2017.02.043>, <http://www.sciencedirect.com/science/article/pii/S0012821X1730119X>, 2017.
- Leinweber, V. T. and Jokat, W.: Is there continental crust underneath the northern Natal Valley and the Mozambique Coastal Plains?, *Geophysical Research Letters*, 38, n/a–n/a, <https://doi.org/10.1029/2011GL047659>, <http://doi.wiley.com/10.1029/2011GL047659>, 2011.
- Leinweber, V. T. and Jokat, W.: The Jurassic history of the Africa–Antarctica corridor — new constraints from magnetic data on the conjugate continental margins, *Tectonophysics*, 530–531, 87–101, <https://doi.org/10.1016/j.tecto.2011.11.008>, <http://linkinghub.elsevier.com/retrieve/pii/S0040195111004641>, 2012.
- Leprêtre, A., Schnürle, P., Evain, M., Verrier, F., Moorcroft, D., Clarens, P. d., Corela, C., Afilhado, A., Loureiro, A., Leroy, S., d’Acremont, E., Thompson, J., Aslanian, D., and Moulin, M.: Deep Structure of the North Natal Valley (Mozambique) Using Combined Wide-Angle and Reflection Seismic Data, *Journal of Geophysical Research: Solid Earth*, 126, e2020JB021171, <https://doi.org/https://doi.org/10.1029/2020JB021171>, <https://agupubs.onlinelibrary.wiley.com/doi/abs/10.1029/2020JB021171>, <https://agupubs.onlinelibrary.wiley.com/doi/pdf/10.1029/2020JB021171>, 2021.

- Li, H., Tang, Y., Moulin, M., Aslanian, D., Evain, M., Schnurle, P., Leprêtre, A., and Li, J.: Seismic evidence for crustal architecture and stratigraphy of the Limpopo Corridor: New insights into the evolution of the sheared margin offshore southern Mozambique, *Marine Geology*, 435, 106 468, <https://doi.org/10.1016/j.margeo.2021.106468>, <https://linkinghub.elsevier.com/retrieve/pii/S0025322721000505>, 2021.
- 750 Loureiro, Afilhado, A., Matias, L., Moulin, M., and Aslanian, D.: Monte Carlo approach to assess the uncertainty of wide-angle layered models: Application to the Santos Basin, Brazil, *Tectonophysics*, 683, 286–307, <https://doi.org/10.1016/j.tecto.2016.05.040>, <https://linkinghub.elsevier.com/retrieve/pii/S0040195116301767>, 2016.
- Loureiro, Schnürle, P., Klingelhöfer, F., Afilhado, A., Pinheiro, J., Evain, M., Gallais, F., Dias, N. A., Rabineau, M., Baltzer, A., Benabdelouahed, M., Soares, J., Fuck, R., Cupertino, J. A., Viana, A., Matias, L., Moulin, M., Aslanian, D., Morvan, L., Mazé, J. P., Pierre, D.,
- 755 Roudaut-Pitel, M., Rio, I., Alves, D., Barros Junior, P., Biari, Y., Corela, C., Crozon, J., Duarte, J. L., Ducatel, C., Falcão, C., Fernagu, P., Vinicius Aparecido Gomes de Lima, M., Le Piver, D., Mokeddem, Z., Pelleau, P., Rigoti, C., Roest, W., and Roudaut, M.: Imaging exhumed lower continental crust in the distal Jequitinhonha basin, Brazil, *Journal of South American Earth Sciences*, 84, 351–372, <https://doi.org/10.1016/j.jsames.2018.01.009>, <http://www.sciencedirect.com/science/article/pii/S0895981117302948>, 2018.
- Ludwig, W. J., Nafe, J. E., Simpson, E. S. W., and Sacks, S.: Seismic-refraction measurements on the Southeast African Continental Margin, *Journal of Geophysical Research*, 73, 3707–3719, <https://doi.org/10.1029/JB073i012p03707>, <https://agupubs.onlinelibrary.wiley.com/doi/abs/10.1029/JB073i012p03707>, 1968.
- 760 Ludwig, W. J., Nafe, J. E., and Drake, C.: Seismic refraction, in: *The Sea 4 (Part 1)*, pp. 53–84, 1970.
- Mahanjane, E. S.: A geotectonic history of the northern Mozambique Basin including the Beira High – A contribution for the understanding of its development, *Marine and Petroleum Geology*, 36, 1–12, <https://doi.org/10.1016/j.marpetgeo.2012.05.007>, <http://www.sciencedirect.com/science/article/pii/S0264817212001274>, 2012.
- 765 Martin, A. K. and Hartnady, C. J. H.: Plate tectonic development of the south west Indian Ocean: A revised reconstruction of East Antarctica and Africa, *Journal of Geophysical Research: Solid Earth*, 91, 4767–4786, <https://doi.org/https://doi.org/10.1029/JB091iB05p04767>, <https://agupubs.onlinelibrary.wiley.com/doi/abs/10.1029/JB091iB05p04767>, [_eprint: https://agupubs.onlinelibrary.wiley.com/doi/pdf/10.1029/JB091iB05p04767](https://agupubs.onlinelibrary.wiley.com/doi/pdf/10.1029/JB091iB05p04767), 1986.
- 770 Mascle, J. and Blarez, E.: Evidence for transform margin evolution from the Ivory Coast–Ghana continental margin, *Nature*, 326, 378–381, <https://doi.org/10.1038/326378a0>, <https://www.nature.com/articles/326378a0>, 1987.
- Mougenot, D., Recq, M., Virlogeux, P., and Lepvrier, C.: Seaward extension of the East African Rift, *Nature*, 321, 599–603, <https://doi.org/10.1038/321599a0>, <https://www.nature.com/articles/321599a0>, number: 6070 Publisher: Nature Publishing Group, 1986.
- Moulin, M. and Aslanian, D.: PAMELA-MOZ03 cruise report. <http://dx.doi.org/10.17600/16001600>, Tech. rep., 2016.
- 775 Moulin, M. and Evain, M.: PAMELA-MOZ05 cruise report, <http://dx.doi.org/10.17600/16009500>, Tech. rep., 2016.
- Moulin, M., Aslanian, D., Olivet, J.-L., Contrucci, I., Matias, L., Géli, L., Klingelhoefer, F., Nouzé, H., Réhault, J.-P., and Unternehr, P.: Geological constraints on the evolution of the Angolan margin based on reflection and refraction seismic data (ZaïAngo project), *Geophysical Journal International*, 162, 793–810, <https://doi.org/10.1111/j.1365-246X.2005.02668.x>, <https://academic.oup.com/gji/article-lookup/doi/10.1111/j.1365-246X.2005.02668.x>, 2005.
- 780 Moulin, M., Klingelhoefer, F., Afilhado, A., Aslanian, D., Schnurle, P., Nouzé, H., Rabineau, M., Beslier, M.-O., and Feld, A.: Deep crustal structure across a young passive margin from wide-angle and reflection seismic data (The SARDINIA Experiment) – I. Gulf of Lion’s margin, *Bulletin de la Société Géologique de France*, 186, 309–330, <https://doi.org/10.2113/gssgfbull.186.4-5.309>, <https://pubs.geoscienceworld.org/sgf/bsgf/article/186/4-5/309/285714/Deep-crustal-structure-across-a-young-passive>, 2015.

- Moulin, M., Aslanian, D., Evain, M., Leprêtre, A., Schnurle, P., Verrier, F., Thompson, J., Clarens, P. D., Leroy, S., and Dias, N.: Gondwana
785 breakup: Messages from the North Natal Valley, *Terra Nova*, 32, 205–214, <https://doi.org/10.1111/ter.12448>, <https://onlinelibrary.wiley.com/doi/abs/10.1111/ter.12448>, 2020.
- Mueller, C. O. and Jokat, W.: Geophysical evidence for the crustal variation and distribution of magmatism along the central coast of
Mozambique, *Tectonophysics*, 712–713, 684–703, <https://doi.org/10.1016/j.tecto.2017.06.007>, <https://linkinghub.elsevier.com/retrieve/pii/S0040195117302536>, 2017.
- 790 Mueller, C. O. and Jokat, W.: The initial Gondwana break-up: A synthesis based on new potential field data of the Africa-
Antarctica Corridor, *Tectonophysics*, 750, 301–328, <https://doi.org/10.1016/j.tecto.2018.11.008>, <https://linkinghub.elsevier.com/retrieve/pii/S0040195118303858>, 2019.
- Mueller, C. O., Jokat, W., and Schreckenberger, B.: The crustal structure of Beira High, central Mozambique—Combined investigation
of wide-angle seismic and potential field data, *Tectonophysics*, 683, 233–254, <https://doi.org/10.1016/j.tecto.2016.06.028>, <http://www.sciencedirect.com/science/article/pii/S0040195116302414>, 2016.
- 795 Pavlis, N. K., Holmes, S. A., Kenyon, S. C., and Factor, J. K.: The development and evaluation of the Earth Gravitational Model 2008
(EGM2008), *Journal of Geophysical Research: Solid Earth*, 117, <https://doi.org/10.1029/2011JB008916>, <https://agupubs.onlinelibrary.wiley.com/doi/abs/10.1029/2011JB008916>, 2012.
- Piqué, A., Laville, E., Chotin, P., Chorowicz, J., Rakotondraompiana, S., and Thouin, C.: L’extension à Madagascar du Néogène à l’Actuel:
800 arguments structuraux et géophysiques, *Journal of African Earth Sciences*, 28, 975–983, [https://doi.org/10.1016/S0899-5362\(99\)00073-1](https://doi.org/10.1016/S0899-5362(99)00073-1), <https://www.sciencedirect.com/science/article/pii/S0899536299000731>, 1999.
- Reeves, C. V., Teasdale, J. P., and Mahanjane, E. S.: Insight into the Eastern Margin of Africa from a new tectonic model of the Indian Ocean,
Geological Society, London, Special Publications, 431, 299–322, <https://doi.org/10.1144/SP431.12>, <http://sp.lyellcollection.org/lookup/doi/10.1144/SP431.12>, 2016.
- 805 Reid: Effects of lithospheric flow on the formation and evolution of a transform margin, *Earth and Planetary Science Letters*, 95, 38–52,
[https://doi.org/10.1016/0012-821X\(89\)90166-0](https://doi.org/10.1016/0012-821X(89)90166-0), <http://www.sciencedirect.com/science/article/pii/0012821X89901660>, 1989.
- Reid and Jackson: A review of three transform margins off eastern Canada, *Geo-Marine Letters*, 17, 87–93,
<https://doi.org/10.1007/s003670050012>, <https://doi.org/10.1007/s003670050012>, 1997.
- Riedel, S., Jacobs, J., and Jokat, W.: Interpretation of new regional aeromagnetic data over Dronning Maud Land (East
810 Antarctica), *Tectonophysics*, 585, 161–171, <https://doi.org/10.1016/j.tecto.2012.10.011>, <http://www.sciencedirect.com/science/article/pii/S0040195112006658>, 2013.
- Salman, G. and Abdula, I.: Development of the Mozambique and Ruvuma sedimentary basins, offshore Mozambique, *Sedimentary Geology*,
96, 7–41, [https://doi.org/10.1016/0037-0738\(95\)00125-R](https://doi.org/10.1016/0037-0738(95)00125-R), <http://linkinghub.elsevier.com/retrieve/pii/003707389500125R>, 1995.
- Sandwell, D. T., Müller, R. D., Smith, W. H. F., Garcia, E., and Francis, R.: New global marine gravity model from CryoSat-2 and Jason-1
815 reveals buried tectonic structure, *Science*, 346, 65–67, <https://doi.org/10.1126/science.1258213>, <https://science.sciencemag.org/content/346/6205/65>, 2014.
- Saria, E., Calais, E., Stamps, D. S., Delvaux, D., and Hartnady, C. J. H.: Present-day kinematics of the East African Rift, *Journal of Geophys-
ical Research: Solid Earth*, 119, 3584–3600, <https://doi.org/10.1002/2013JB010901>, <http://doi.wiley.com/10.1002/2013JB010901>, 2014.
- Scheinert, M., Ferraccioli, F., Schwabe, J., Bell, R., Studinger, M., Damaske, D., Jokat, W., Aleshkova, N., Jordan, T., Leitchenkov, G.,
820 Blankenship, D. D., Damiani, T. M., Young, D., Cochran, J. R., and Richter, T. D.: New Antarctic gravity anomaly grid for enhanced

- geodetic and geophysical studies in Antarctica, *Geophysical Research Letters*, 43, 600–610, <https://doi.org/10.1002/2015GL067439>, <https://onlinelibrary.wiley.com/doi/abs/10.1002/2015GL067439>, 2016.
- Schnürle, P., Leprêtre, A., Verrier, F., Evain, M., Aslanian, D., De Clarens, P., Dias, N. A., Loureiro, A., Leroy, S., and Moulin, M.: Crustal structure of the Natal Valley from combined wide-angle and reflection seismic data (MOZ3/5 cruise), South Mozambique Margin, in: 18th International SEISMIX Symposium, Cracow, Poland, 2018.
- Senkans, A., Leroy, S., d'Acremont, E., Castilla, R., and Despinos, F.: Polyphase rifting and break-up of the central Mozambique margin, *Marine and Petroleum Geology*, 100, 412–433, <https://doi.org/10.1016/j.marpetgeo.2018.10.035>, <https://linkinghub.elsevier.com/retrieve/pii/S0264817218304410>, 2019.
- Smith, W. H. F. and Sandwell, D. T.: Global Sea Floor Topography from Satellite Altimetry and Ship Depth Soundings, *Science*, 277, 1956–1962, <https://doi.org/10.1126/science.277.5334.1956>, <https://www.sciencemag.org/lookup/doi/10.1126/science.277.5334.1956>, 1997.
- Stockwell, J. W.: The CWP/SU: Seismic Unix package, *Computers & Geosciences*, 25, 415–419, 1999.
- Teyssier, C., Tikoff, B., and Markley, M.: Oblique plate motion and continental tectonics, *Geology*, 23, 447–450, [https://doi.org/10.1130/0091-7613\(1995\)023<0447:OPMACT>2.3.CO;2](https://doi.org/10.1130/0091-7613(1995)023<0447:OPMACT>2.3.CO;2), <https://pubs.geoscienceworld.org/gsa/geology/article/23/5/447/206316/Oblique-plate-motion-and-continental-tectonics>, publisher: GeoScienceWorld, 1995.
- Thiéblemont, A., Hernández-Molina, F. J., Miramontes, E., Raissou, F., and Penven, P.: Contourite depositional systems along the Mozambique channel: The interplay between bottom currents and sedimentary processes, *Deep Sea Research Part I: Oceanographic Research Papers*, 147, 79–99, <https://doi.org/10.1016/j.dsr.2019.03.012>, <http://www.sciencedirect.com/science/article/pii/S0967063718303091>, 2019.
- Thompson, J. O., Moulin, M., Aslanian, D., de Clarens, P., and Guillocheau, F.: New starting point for the Indian Ocean: Second phase of breakup for Gondwana, *Earth-Science Reviews*, 191, 26–56, <https://doi.org/10.1016/j.earscirev.2019.01.018>, <http://www.sciencedirect.com/science/article/pii/S0012825218304409>, 2019.
- Tikku, A. A., Marks, K. M., and Kovacs, L. C.: An Early Cretaceous extinct spreading center in the northern Natal valley, *Tectonophysics*, 347, 87–108, [https://doi.org/10.1016/S0040-1951\(01\)00239-6](https://doi.org/10.1016/S0040-1951(01)00239-6), <http://www.sciencedirect.com/science/article/pii/S0040195101002396>, 2002.
- Tozer, B., Watts, A. B., and Daly, M. C.: Crustal structure, gravity anomalies, and subsidence history of the Parnaíba cratonic basin, Northeast Brazil: Structure Parnaíba Cratonic Basin, *Journal of Geophysical Research: Solid Earth*, 122, 5591–5621, <https://doi.org/10.1002/2017JB014348>, <http://doi.wiley.com/10.1002/2017JB014348>, 2017.
- Tsang-Hin-Sun, E., Evain, M., Julia, J., Lamarque, G., and Schnurle, P.: Crustal seismic structure and anisotropy of Madagascar and south-eastern Africa using receiver function harmonics: interplay of inherited local heterogeneities and current regional stress, *Geophysical Journal International*, <https://doi.org/10.1093/gji/ggab118>, <https://doi.org/10.1093/gji/ggab118>, 2021.
- Vormann, M., Franke, D., and Jokat, W.: The crustal structure of the southern Davie Ridge offshore northern Mozambique – A wide-angle seismic and potential field study, *Tectonophysics*, 778, 228–370, <https://doi.org/10.1016/j.tecto.2020.228370>, <http://www.sciencedirect.com/science/article/pii/S0040195120300536>, 2020.
- Watkeys, M.: Development of the Lebombo rifted volcanic margin of southeast Africa, in: *Volcanic Rifted Margins*, Geological Society of America, <https://doi.org/10.1130/0-8137-2362-0.27>, <https://pubs.geoscienceworld.org/books/book/515/chapter/3801010>, 2002.
- Watremez, L., Leroy, S., d'Acremont, E., Roche, V., Leprêtre, A., Verrier, F., Aslanian, D., Dias, N. A., Afilhado, A., Schnürle, P., Castilla, R., Despinos, F., and Moulin, M.: The Limpopo magmatic transform margin (South Mozambique) – Part 1: insights from deep-structure seismic imaging, Under reviews at *Tectonics*.

- Watts, A. B.: Gravity anomalies, flexure and crustal structure at the Mozambique rifted margin, *Marine and Petroleum Geology*, 18, 445–455, [https://doi.org/10.1016/S0264-8172\(00\)00079-9](https://doi.org/10.1016/S0264-8172(00)00079-9), <http://www.sciencedirect.com/science/article/pii/S0264817200000799>, 2001.
- 860 Wessel, P. and Smith, W. H. F.: New, improved version of Generic Mapping Tools released, *EOS Trans. Amer. Geophys. U.*, 79, 579, 1998.
- White, R. S., McKenzie, D., and O’Nions, R. K.: Oceanic crustal thickness from seismic measurements and rare earth element inversions, *Journal of Geophysical Research*, 97, 19 683, <https://doi.org/10.1029/92JB01749>, <http://doi.wiley.com/10.1029/92JB01749>, 1992.
- Wiles, E., Green, A., Watkeys, M., Jokat, W., and Krockner, R.: Anomalous seafloor mounds in the northern Natal Valley, southwest Indian Ocean: Implications for the East African Rift System, *Tectonophysics*, 630, 300–312, <https://doi.org/10.1016/j.tecto.2014.05.030>, <http://www.sciencedirect.com/science/article/pii/S0040195114003035>, 2014.
- 865 Zelt, C. A. and Smith, R. B.: Seismic traveltimes inversion for 2-D crustal velocity structure, *Geophysical Journal International*, 108, 16–34, 1992.

Appendix A

Table A1. Refracted (left) and reflected (right) phase names for MZ3 profile, number of explained events, residual mean-squares in s, and normalized chi-squared values

phase	npts	Trms	χ^2	phase	npts	Trms	χ^2
Pw	3453	0.022	0.613				
Ps1	100	0.036	1.196	Ps2P	681	0.037	0.160
Ps2	818	0.029	1.198	Ps3P	1237	0.033	0.195
Ps3	1336	0.035	1.454	Psv1P	3037	0.037	0.194
Psv1	1547	0.031	0.800	Psv2P	1836	0.038	0.350
Psv2	2314	0.043	1.326	Pg1P	2294	0.063	0.578
Pg1	6353	0.055	1.256	Pg2P	4497	0.057	0.463
Pg2	9062	0.049	0.467	Pg3P	6140	0.061	0.326
Pg3	1832	0.068	0.317	Pg4P	5345	0.092	0.891
Pg4	947	0.051	0.170	Pg5P	4790	0.089	0.695
Pn1	1528	0.101	0.629	PmP	4296	0.082	0.444
Pn2	157	0.144	0.899	Pm2P	1303	0.130	1.034

Table A2. OBS names and distance along MZ3 model, phase propagation direction, number of explained events, residual mean-square in s, and normalized chi-squared value.

OBS	shot	dir	npts	Trms	χ^2	dir	npts	Trms	χ^2
MZ3OBS01	0.000	-1	444	0.053	1.326	1	788	0.067	0.741
MZ3OBS02	12.406	-1	561	0.101	1.592	1	653	0.092	3.225
MZ3OBS03	24.744	-1	358	0.053	0.840	1	563	0.059	0.405
MZ3OBS04	35.074	-1	419	0.062	0.785	1	510	0.081	0.962
MZ3OBS05	47.568	-1	480	0.081	1.570	1	1117	0.067	0.382
MZ3OBS06	60.108	-1	535	0.071	0.652	1	461	0.046	0.641
MZ3OBS07	72.457	-1	914	0.079	0.878	1	1571	0.063	0.231
MZ3OBS08	84.855	-1	610	0.060	0.388	1	1352	0.051	0.360
MZ3OBS09	97.287	-1	768	0.065	0.514	1	1181	0.085	0.584
MZ3OBS10	109.730	-1	578	0.043	0.402	1	1268	0.075	0.830
MZ3OBS11	122.245	-1	605	0.053	0.576	1	1428	0.069	0.346
MZ3OBS12	134.629	-1	551	0.041	0.430	1	1528	0.070	0.363
MZ3OBS13	147.166	-1	1041	0.036	0.336	1	1410	0.053	0.383
MZ3OBS14	159.692	-1	845	0.044	0.419	1	1032	0.049	0.362
MZ3OBS15	172.186	-1	491	0.043	0.673	1	1660	0.103	0.910
MZ3OBS16	186.020	-1	1262	0.058	0.723	1	1263	0.048	0.299
MZ3OBS17	197.187	-1	1565	0.055	0.367	1	1344	0.051	0.697
MZ3OBS18	209.733	-1	1383	0.039	0.301	1	1427	0.064	0.550
MZ3OBS19	222.190	-1	1324	0.045	0.301	1	1149	0.074	0.755
MZ3OBS20	234.697	-1	1430	0.059	0.440	1	1023	0.076	0.568
MZ3OBS21	247.110	-1	1481	0.079	0.701	1	1124	0.054	0.459
MZ3OBS22	259.541	-1	1803	0.057	0.370	1	872	0.057	0.446
MZ3OBS23	271.942	-1	1699	0.062	0.454	1	766	0.061	1.460
MZ3OBS24	284.437	-1	1656	0.053	0.323	1	812	0.045	0.474
MZ3OBS25	296.936	-1	1722	0.076	0.925	1	767	0.059	0.938
MZ3OBS26	309.420	-1	1692	0.067	0.778	1	660	0.073	1.335
MZ3OBS27	321.914	-1	958	0.079	0.691	1	989	0.063	0.660
MZ3OBS28	334.449	-1	915	0.109	1.204	1	1083	0.074	0.484
MZ3OBS29	346.948	-1	781	0.115	1.727	1	1211	0.068	0.885
MZ3OBS30	359.463	-1	658	0.040	0.654	1	1078	0.048	0.575
MZ3OBS31	372.017	-1	1028	0.081	0.920	1	883	0.061	1.136
MZ3OBS32	384.520	-1	943	0.062	1.108	1	813	0.059	0.656

Appendix B: MZ3 uncertainties estimation

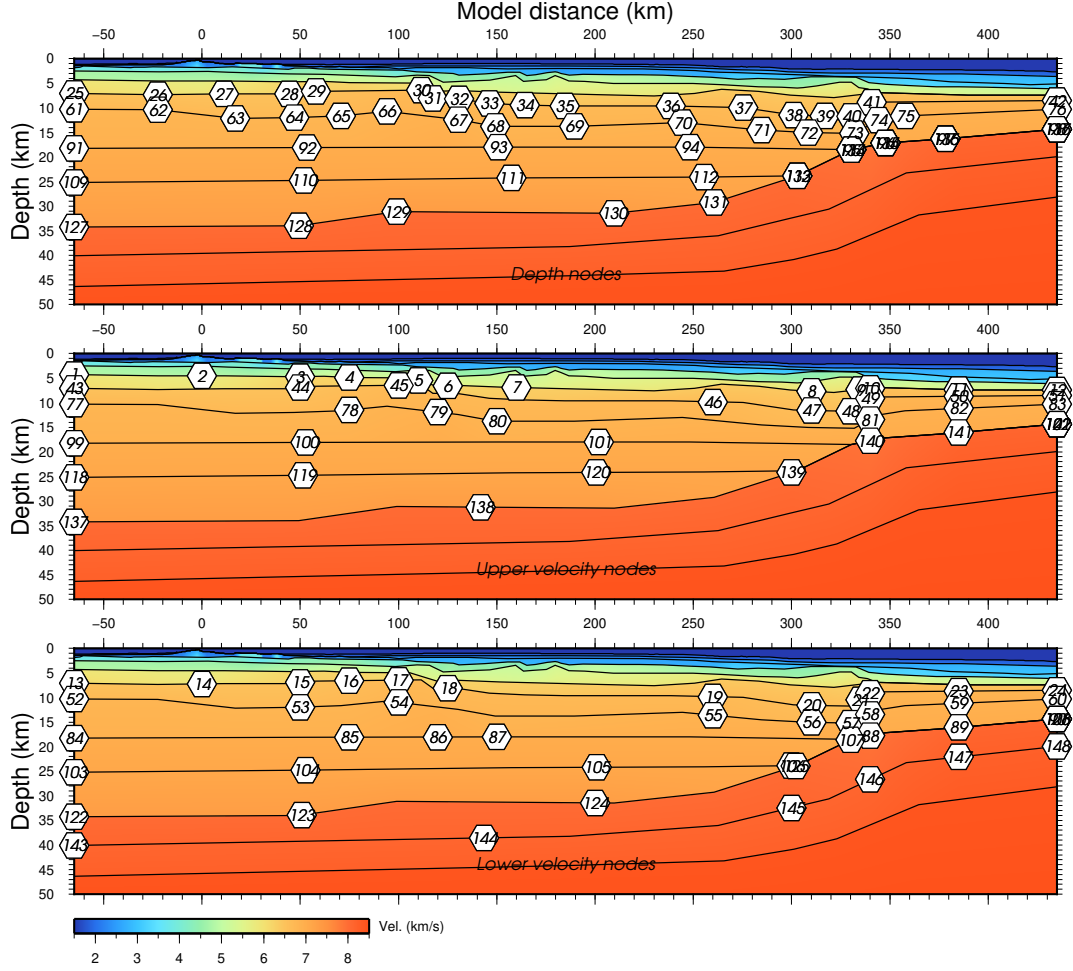


Figure B1. MZ3 final velocity model with parameter selection (white hexagons) for Vmontecarlo. Top panels: depth parameters; middle panels: top of layer velocity parameters; and bottom panels: base of layer velocity parameters. Interfaces indicated by black lines and velocities colored according to color.

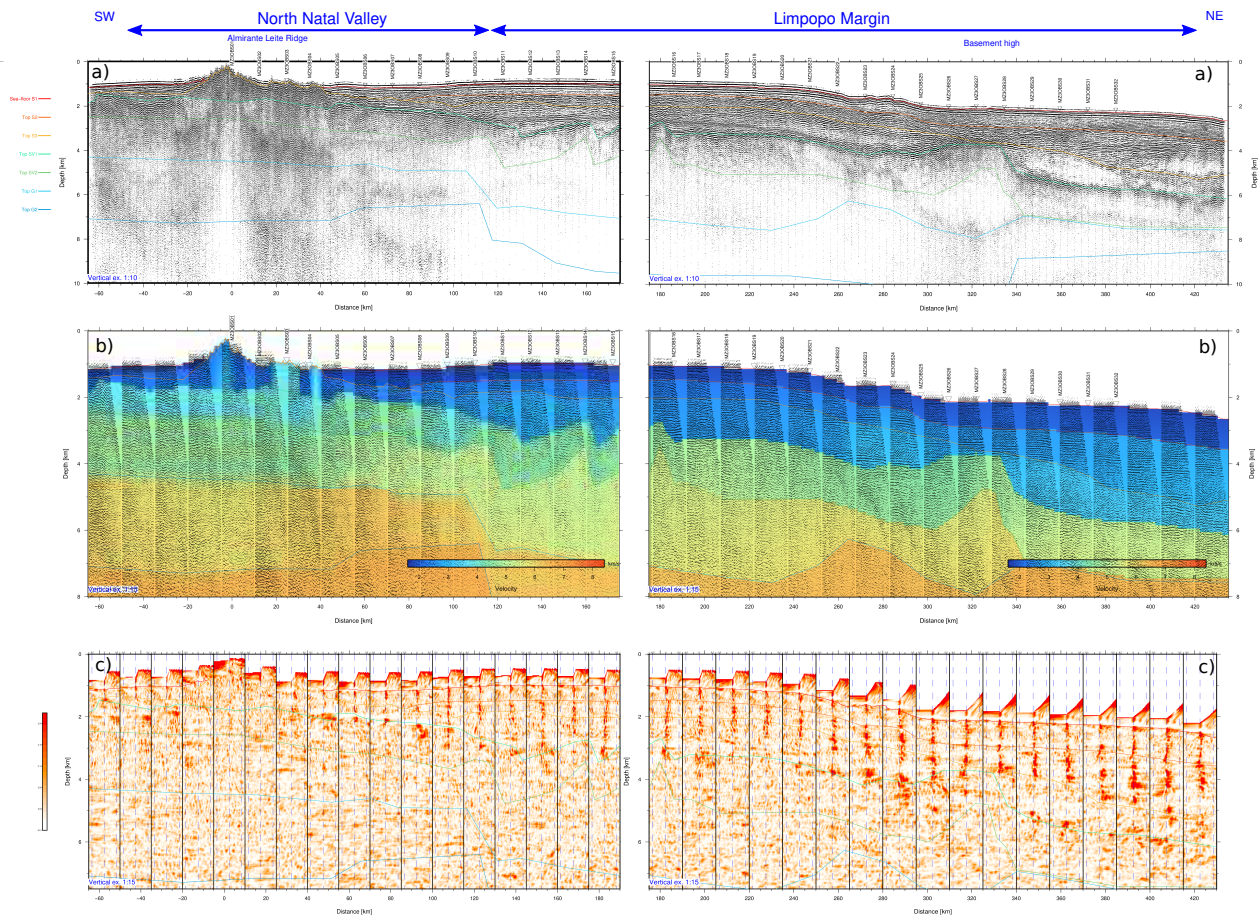


Figure C1. Pre-stack depth migration of MCS MZ3 profile. Left: SW portion ; right: NE portion. a) PSDM record section. The intersections with the MOZ35 dataset are indicated by red line. Vertical exaggeration is 1:10. b) Residual move-out. c) Semblance plot of the RMO. Common image gathers are spaced every 7.5 km. Vertical exaggeration is 1:15. Model's interfaces are represented with continuous lines.